QUASICRYSTALS AS CATALYSTS FOR THE STEAM REFORMING OF METHANOL

Samuel Coates
200782475
MPhys Project

Supervised by

Hem Raj Sharma
Surface Science Research

University of Liverpool
2014/2015

DECLARATION

I, Samuel Coates, confirm that the work submitted in this thesis is my own, and that appropriate credit has been given where reference is made to the work of others.

Signature: ____________________________

Date: ____________________________

ACKNOWLEDGEMENTS

First and foremost, I would like to thank my Father, Phil, for being the role model I need, and whose words inspired me to start ‘something beautiful’. To my sister, Ruby - for being my best friend and whose own incredible determination shaped my path, convincing me to not take the easy route. To Shelly, my step-mother, whose sheer optimism and clear-headedness in the face of difficulty have always kept my head above water. To Hannah, my invaluable partner, your unending support has given me the ability to do things I never believed I could be capable of. To my mother, Gina, who has taught me the value of responsibility and has given me the will to succeed.

To my close friends - Emma Beasor, Joe Purves, Tom Neal, Joe Lindsay, Niall Young, Grace Loxley, Rachel Gilroy (whose order is, of course, arbitrary), I thank you for our irreplaceable time at University, long may our friendships last.

To Dr. Paul Unsworth, who collected the XPS data for me and provided me with a friendly face and helpful advice. Finally, I thank Dr. Hem Raj Sharma - who in addition to giving me the support to complete this work, has given me the opportunity to continue my studies as a PhD student.

Abstract

A study on the subject of surface science techniques and their use in analysis of potential applications for quasicrystals is presented. Using X-ray Photoelectric Spectroscopy (XPS), core level electron peak positions have been investigated to assess the effect of icosahedral ((i) - ordered, but aperiodic) structure and oxide formation on the surface of i-Al-Cu-Fe and i-Al-Pd-Mn quasicrystals. Al_2O_3 formed at the expense of any other oxides, leading to binding energy shifts for Al2p on both QCs. Compositional analysis conducted upon both QCs concluded that a passivity layer of this oxide segregated from the surface which consequently dominated the composition calculations, giving high Al percentages. Sputtering removed this segregated layer - giving Al percentage values lower than the as-grown compositions ($Al_{63}Cu_{24}Fe_{13}$, $Al_{70}Pd_{20}Mn_{10}$ respectively) - a result expected when compared to previous studies. This effect of decreasing aluminium at the surface was seen for both QCs, meaning an increase in the more catalytically active components was seen (Cu and Pd, respectively).

Additionally, Al2p peak shifts were witnessed without oxidation - leading to the tentative suggestion that these shifts are due to charge transfer between elements at the surface of the quasicrystals. Charge transfer shifts were also seen in the annealed Al-Pd-Mn quasicrystal for the Pd3d peaks - a phenomena that has previously been discovered in previous studies.

Due to the nature of UHV experiments (the necessity of high precision measurements and an environment which breeds breakages and delays) the initial aim of this experiment (depositing methanol at the surface of these QCs) have not been completed - yet the results obtained have leant valuable experience to the author. The project shall be continued in the future as part of the author's PhD studies.

Contents

Chapter 1

Introduction

Formally observed in 1982, quasicrystalline structure can be described by a crystal (typically composed of inter-metallic compounds) which possesses long-range order, without translational symmetry and exhibits classically forbidden orders of rotational symmetry such as five-fold and ten-fold [1]. These quasicrystals (QCs) have only been observed as a natural material once (discovered inside a meteorite [2]), rather, they are commonly synthesized to produce desirable properties. Most QCs contain catalytically active elements (such as Cu, Fe, Pd) and show different physical properties to classically arranged intermetallic compounds (high hardness, low surface energies etc.). Although theoretically useful due to these properties, QCs are yet to be used widely in industry and have so far been restricted to a narrow range of applications. However, one such quasicrystal has been identified as a potentially market-changing catalyst: Al-Cu-Fe.

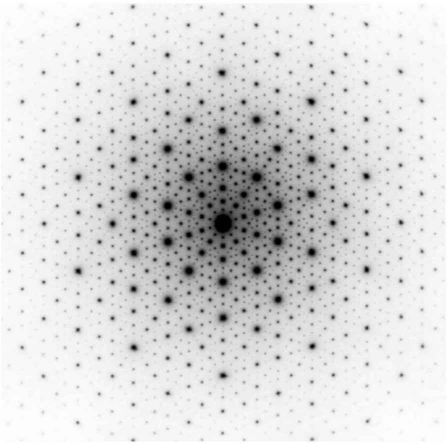

Figure 1.1: Diffraction pattern showing classically forbidden orders of symmetry, from an Al-Pd-Mn quasicrystal [3].

Typically, commercial catalysts contain rare elements, rendering them expensive; a cheaper (yet equally as productive) catalyst would provide an incredible boost to the catalytic industry. Al, Cu and Fe are all relatively cheap and easily attainable when compared to heavily used elements within the catalysis industry (Pt, for example). With this in mind, work previously undertaken by Tsai *et al.* with the Al-Cu-Fe quasicrystal has changed the impetus of QC research, with its base now firmly set in catalysis [4]. Their work on the use of the Al-Cu-Fe as a catalyst in the steam reforming of methanol (SRM) has led to a raft of further research into this reaction, including the procedure documented in this thesis.

Following on from these studies, the experiment explained within aims to review the comparative reactivity of un-leached and leached quasicrystals towards organic molecules (i.e. methanol), in an effort to understand why steam reforming takes place in the presence of certain quasicrystals and how we can optimise it. Presented, therefore, is a research study performed upon i-Al-Cu-Fe and i-Al-Pd-Mn quasicrystals (noted without the icosahedral (i) from now on), investigating their use as a catalyst for steam reforming of methanol. Specifically, the surface of the single grain Al-Cu-Fe QC will be studied to assess why it is such an active catalyst for this reaction. Then, in addition, the Al-Pd-Mn QC will be investigated as to whether it can also be used as such a catalyst. Both samples shall be sputtered at first, to provide a 'rough' surface for the methanol to stick and decompose at. Sputtering removes the quasicrystalline structure of the surface, so, the samples will be then annealed until QC structure is restored - and the methanol deposition will be tested again. If deposition is successful, the surfaces will contain organic chemi and physisorbed species that can be readily analysed to ascertain the manner in which the methanol is decomposed.

The following introductory sections will detail past studies on the subject that will give an insight into the motivation behind this study, as well as a comprehensive theoretical explanation of the science behind quasicrystalline structure.

1.1 Steam Reforming of Methanol (SRM)

Hydrogen produced using natural gas is a commercial market that is now worth over $100 billion, with the primary method of said production via the steam reforming of hydrocarbons [5]. Catalysts in general can be used to speed up chemical reactions, or to increase the volume/amount of desired product. Increasing the quality or efficiency of catalysts whilst simultaneously lowering the cost of producing said catalysts would obviously present a large advantage to the hydrogen production industry.

The steam reforming of methanol is a specific reaction to the general hydrocarbon reaction (methanol is an alcohol derivative of methane - a hydrocarbon) and is shown below:

$$CH_3OH + H_2O = 3H_2 + CO_2 \tag{1.1}$$

where CH_3OH is methanol. Simply, (1.1) occurs when, at high temperatures ($\sim$ 500K [4]) and in the presence of a catalyst, steam reacts with methanol and produces hydrogen and carbon dioxide.

Previous research undertaken has looked at the usage of quasicrystals (specifically Al-Cu-Fe) as a catalyst for this reaction. Now, these QC's are reactive, but they can be treated to further increase their catalytic activity. One particular method of treating a catalyst was introduced by M. Raney [6] who used the selective leaching of Ni-Al and Ni-Si alloys with NaOH to obtain highly active Ni catalysts [7]. Thus, a catalyst that has been treated in this manner is dubbed a 'Raney Catalyst'. Tsai *et al.* reported the

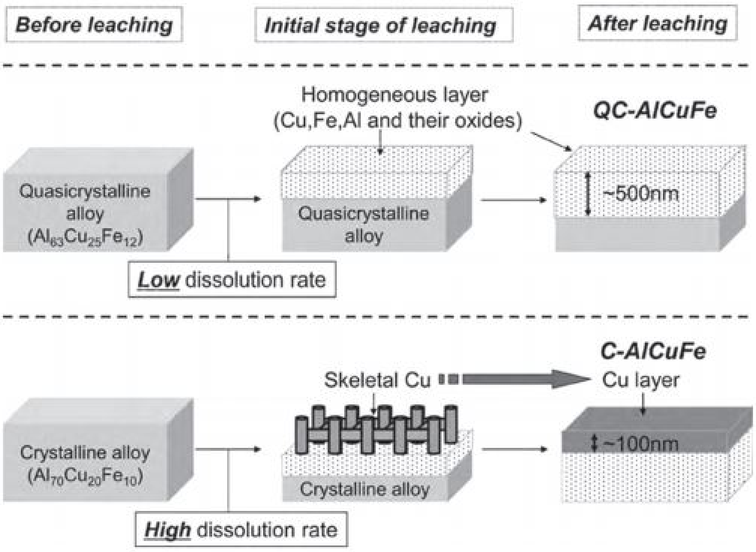

Figure 1.2: The comparison between quasicrystalline and crystalline Al-Cu-Fe behaviour to being leached. The dissolution rate refers to the rate at which Al is leached away.

usage of Al-Cu-Fe as a catalyst after performing the Raney method, citing its 'excellent activity following leaching, producing H_2 at a rate of 235 ml/g per minute' [4]. This production rate is comparable to industrial standard catalysts, with the advantage of low cost, ease of production and brittle nature (allowing high surface area). Within their paper, they also noted that the leaching removes Al oxides present at the surfacea, and that the Al oxidation plays a role in the catalytic reaction. Further to this, they noticed Cu nanoparticles formed at the surface due to the leaching of the QC, and identified these nanoparticles as the origin of the activity.

In further studies, these particles were found to be resistant to sintering, a process whereby many small particles merge to form one large particle - a widespread problem in the catalyst industry [8]. This suppression of sintering has been assigned to the presence of iron at the surface (Fe is immiscible with Cu [7]), as well as the interaction between the particles and the quasicrystalline structure. The structure of the crystal is incredibly important in the formation of these particles: in an experiment that compared the leaching of QC Al-Cu-Fe and conventionally crystalline Al-Cu-Fe, Tanabe *et al.* found that the crystallised alloy formed a skeletal Cu formation when leached (see fig. 1.2), as opposed to a particular form as seen in the QC [9]. It can be proposed, then, that because the particular nature of the QC surface is responsible for the catalytic activity, Raney QC catalysts have a distinct advantage over standard Raney catalysts.

The leaching process and its effects on the QC have then been further scrutinised by M.Lowe *et al.*, with a prepared model Al-Cu-Fe catalyst, i.e. a single grain sample that can be used to investigate the surface changes (covered further in section **2.3**)[10]. The research undertaken by M.Lowe *et al* found that leaching treatments over different periods of time preferentially remove Al, producing a 'layer consisting of Fe, Cu, and their native oxides', whilst 'the quasicrystalline bulk structure beneath remains unchanged' - again, see fig. 1.2. These findings re-iterate what Tanabe *et al.* discovered when comparing QC Al-Cu-Fe and its crystalline form [9]. In essence, the leaching causes the surface composition of the QC to change, resulting in increased iron III oxide (Fe_2O_3) and copper I oxide (Cu_2O), taking the form of nanoparticles (including elemental Cu, Fe). It is believed that these nanoparticles are responsible for the catalytic reactions.

Before the bulk of the questions outlined within the introduction are assessed, a theoretical introduction to the science behind this experiment will be given, with a view to presenting an overall understanding of the steps undertaken.

1.2 Crystal Structure

Crystallography - the study of arrangement of atoms in a crystalline solid - is a science that has been researched for over a 100 years and has hence borne a multitude of discoveries, physical laws and advancements for our understanding of how solids behave. Within 14 years of the discovery of X-rays (1901), the Bragg condition for X-ray diffraction from the surface of a solid had been discovered (both discoveries warranting Nobel prizes for W. Röntgen and W. Bragg Snr, W. Bragg Jnr respectively), advancing a field of physics from non-existence to hot topic within the blink of an eye. Part of the appeal of crystallography (particularly within research) is that the physical structure of crystalline structures - for the most part - follow simple mathematical and geometrical rules that allow the modelling and predicting of the behaviour of these solids. To this end, the classical picture of crystal structure will be explored; the rotational and translational properties of basic crystal structure will be explained, how crystallographic restriction theorem prevents certain rotational orders, and how quasicrystalline structure distorts these rules.

Classical crystal structure can be easily defined by a set of regular periodic arrangement of points in space, all connected by translation vectors [11]:

$$t_n = n_1 t_1 + n_2 t_2 + n_3 t_3 \tag{1.2}$$

where t_i are the fundamental translational vectors and n_i are integer numbers (i = 1, 2, 3). These vectors form what is known as a Bravais lattice, a collection of points created by an infinitely repeating ‘conventional unit cell’ - that is, a cell containing only one lattice point. By supposing vectors **a**, **b** and **c** with angles α, β and γ between them, 14 unique Bravais lattices in 3-dimensional space can be determined by considering the rotational and translational symmetry each unit cell holds. These 14 lattices can be categorised into seven crystal systems of increasing symmetry that result in primitive, base-centred, body-centred and face-centred structures as shown above. Fig. 1.3 shows a set of *discrete* lattices that can be used to describe every kind of physical crystal structure exhibited by solids - apart from quasicrystals. As mentioned above, the lattices shown rely on the translational and rotational symmetry of the unit cells; quasicrystals do not exhibit translational symmetry, and possess forbidden orders of rotational symmetry.

The idea of ‘forbidden’ orders of symmetry can be explained using the crystallographic restriction theorem, which in its basic form is based on an observation that the rotational symmetries of crystals are limited to 2,3,4 and 6-fold. The distinction of a discrete lattice used above is an important one, as discreteness implies that there is a minimum distance

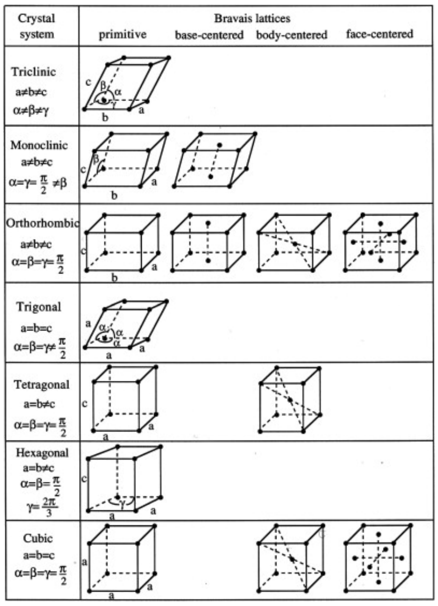

Figure 1.3: Bravais lattice table describing each classical structure dependent on the symmetry of each unit cell [11].

between lattice points and as such, the number of rotational symmetries is finite. More specifically, a rotation symmetry of certain order can move a lattice point through a succession of other lattice points, generating a geometrical shape with coplanar lattice points. However, this statement restricts the order of rotations and number of shapes created (a theorem proved within the appendix (5.1)) to the rotational limits as stated above. A significant point to make here is that these theories restrict the way in which lattices are created *only* i.e. it does not prohibit a 5-fold symmetric assembly from crystallizing, but rather prohibits the formation of a 5-fold symmetric crystal lattice [12].

An easy way to validate this statement is to compare how the rotational symmetry centres behave in quasi and periodic crystalline structure. Within periodic structure, rotations are possible from any one of an infinite number of rotational centres - it is easy to imagine such a system when fig. 1.4 is considered.

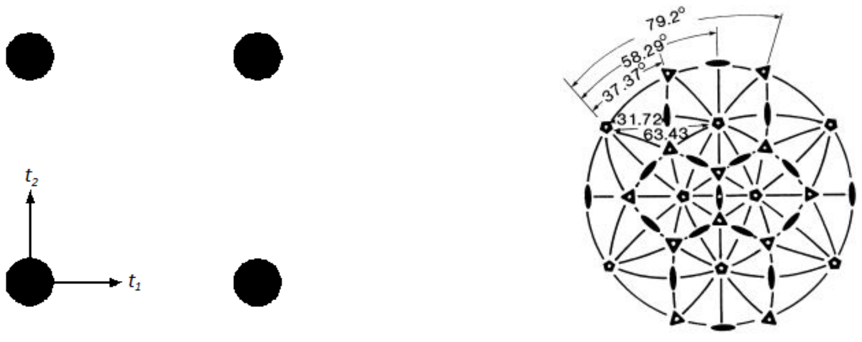

(a) A 2D cubic lattice unit cell.

(b) A symmetry diagram of an icosahedral structure. [1]

Figure 1.4: A rotational symmetry comparison of periodic and quasicrystal.

Fig. 1.4a shows a 2D unit cell used to produce a 2D Bravais lattice. Suppose this cell is infinitely repeated - it becomes clear that any lattice point can be used as a rotational centre. Fig. 1.4b shows a projection of the symmetry elements of an icosahedral group (Al-Cu-Fe and Al-Pd-Mn are both icosahedral QCs. An icosahedron is shown in the appendix (5.2)). This image does not represent a QC unit cell, but illustrates the point that this form of structure has only one point at which there is exact 5-fold symmetry. (Note: icosahedral structures display six fivefold, ten threefold, and fifteen twofold axes of symmetry [1]).

Thus, quasicrystalline structure is 'allowed' to exist in nature and has physical and mathematical reasoning explaining its existence. Perhaps a more direct (and beautiful) example of QC structure is the Penrose tile - the physical manifestation of which is exhibited in Bragg diffraction patterns of QCs (see fig. 1.1). A Penrose tile can be constructed by two types of tile which are then laid down according to 'matching rules' (i.e. rules that specify how these tiles can meet each other at a vertex or edge). Different tiles and matching rules can create many different Penrose tiles. Fig. 1.5 shows a 'decagonal' Penrose tile - this tile is known as the most realistic model for quasicrystalline structure. In physical terms, it has been suggested that (analagous to the two tiles that make up a Penrose tile) atoms that form two or more clusters can exhibit similar structure, with interactions that mimic the 'matching rules' [13]. By studying fig. 1.1 closely, it can be seen how these tiles are physically represented in diffraction patterns (i.e. each vertex is a diffraction spot).

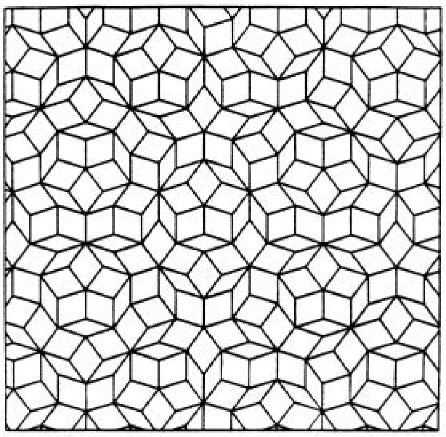

Figure 1.5: An example of a penrose tile [14].

With the motivation behind this study and the theory of quasicrystalline structure covered, the following chapter will detail the main experimental techniques and theories used in this thesis.

Chapter 2

Method

Detailed within this chapter are the steps taken to explore the reactivity of Al-Cu-Fe and Al-Pd-Mn quasicrystals to organic molecules. Before the brunt of the experimental details are presented however, the theory behind data acquisition and the method by which the data will be analysed shall be discussed.

2.1 X-ray Photoelectric Spectroscopy (XPS)

X-ray photoelectric spectroscopy (XPS) is, as the name suggests, spectroscopy based upon the detection of photoelectrons excited by X-rays. The photoelectric effect (a subject which won A.Einstein a Nobel prize) is, in its simplest form, a step process in which an electron initially bound to an atom/ion is ejected by radiation (photons). If the energy of the incident radiation is sufficient, then said electron will be emitted from the bulk of the material as well. This so called 'photoelectron' will then have a kinetic energy - this K.E. is the quantity that is measured and is of a discrete nature. The discreteness of this K.E. is inherently useful as it is a function of the electron's binding energy (B.E.) which, in turn, is characteristic of the element the electron has left [15]. A mathematical formulation that describes this relation is as follows:

$$K.E. = E_p - \phi - B.E. \tag{2.1}$$

where E_p is the energy of the photon and ϕ is the work function of the instrument (minimum energy needed to remove an electron from the instrument). At this point it is worth introducing spectroscopic notation: a method by which a specific integer followed by a specific letter describes a particular electronic state. The integer, quantum number n, refers to the energy level of the atom the electron resides in, with increasing number leading to a decrease in binding energy. The letter (ascending from s, p, d, f, then alphabetically thereafter) describes the quantum number assigned to the orbital angular momentum of the electron ℓ, where s corresponds to $\ell = 0$, p is ℓ=1 etc. Therefore, an electron with $\ell =$ 1 residing in the second lowest energy level of an atom would be noted as: 2p. However, it is entirely possible that electrons within the same atom can have identical values of n and ℓ, leading to 'spin orbit splitting'. Simply, these electrons display a variation in

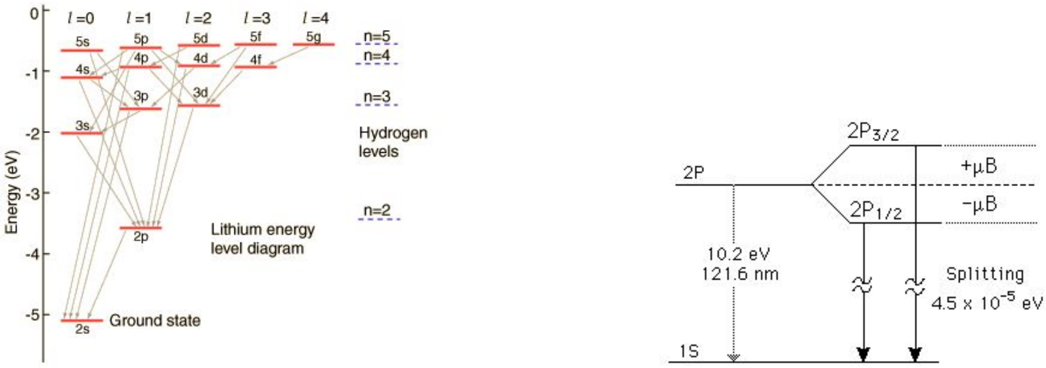

(a) Energy level diagram of Li.

(b) Orbit splitting.

Figure 2.1: Graphical representation of energy levels and spin orbit splitting [16].

energy which can then be signified by the subscript quantum number j, the total angular momentum. So, two 2p electrons are written as: $2p_{1/2}$, $2p_{3/2}$.

In addition to the above photoelectron phenomena, a further physical effect is observed when a sample is irradiated as described: Auger electrons are emitted. Auger electrons are a consequence of an electron from a high level falling into a core level vacancy, emitting energy as it does. Whilst the majority of the time this energy is emitted as a photon, it can however excite a further electron that is then emitted. These Auger electrons do not adhere to equation (2.1), rather, their kinetic energies are as a result of the difference between the two energy levels of the element. Because of this, these electrons are again characteristic of specific elements. Auger electrons are noted in terms of 3 locations, i.e. first letter: initial core hole location, second letter: initial location of relaxing electron, and the third letter: location of second hole. So, for example, Cu LMM.

By taking advantage of such physical properties as the photoelectron effect and Auger electron emission, a K.E./B.E. spectrum of an element or material can be created that displays features that are characteristic of said element/elements within the material. So, to begin the process of collecting these electrons a suitable source of radiation is needed to excite them. Now, as previously stated, XPS is concerned with X-ray radiation - and for a

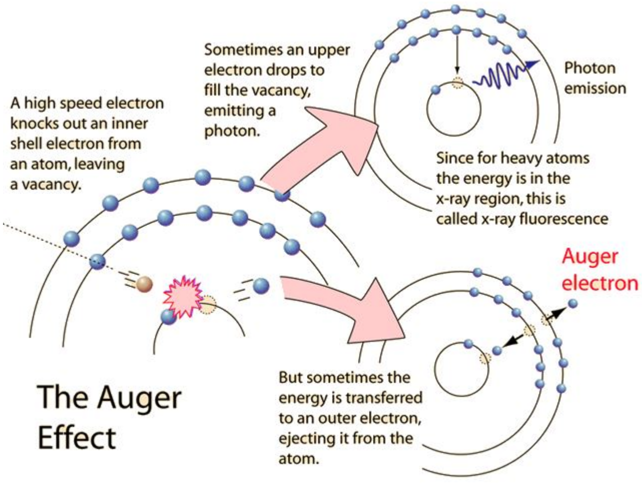

Figure 2.2: Diagram illustrating how Auger electrons are emitted [16].

specific reason. The theory of XPS demands the excitation of core electrons, so the source of radiation used must be sufficiently energetic to excite a large range of core electron energy levels. Photons of this energy fall within the X-ray section of the electromagnetic spectrum, thus, X-ray photoelectron spectroscopy [15].

To produce X-rays, there are two commonly used options - X-ray tubes and synchrotron radiation. For the purpose of this thesis and indeed the experiment contained within, only X-ray tubes will be explored; specifically, monochromatic (one wavelength) sources. The main advantage of using monochromatic sources is that the distribution of the photon energies used is narrow compared to the unfiltered X-rays, this improves the resolution of the photoelectric peaks detected [17]. X-ray tubes produce X-rays via electron bombardment of a metal anode; the choice of the metal used in the anode is important, as it governs the energy of the X-rays created that are then used in the XPS method. The most popular (and indeed used in this experiment) anode material is Al - the radiation it produces is sufficiently energetic and has a minimal spread (i.e. little deviation in energy). However, if these X-rays were then shone directly onto the sample there would still be some deviation in wavelength and hence energy - Al X-rays produced in this manner have an energy of 1486.6 eV with a spread of 0.85 eV. The spread is a cause of concern - it means the X-rays can excite the surrounding medium, as well as the sample under observation, leading to unwanted peaks. To counteract this the X-rays can be focussed using a crystal to reduce the spread - making them monochromatic. The following figure explains how this can be achieved, as well as providing a schematic for the source geometry:

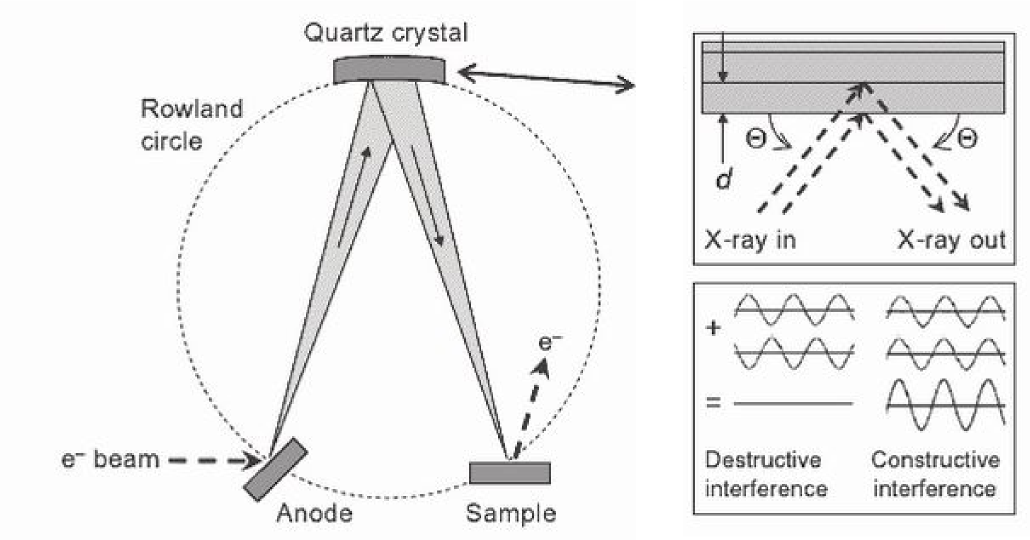

(a) Monochromation process. *(b) Simple diffraction diagram.*

Figure 2.3: Schematic describing the monochromatic process used to focus X-ray energies [15].

To fully explain the process in which X-rays are monochromated, the Bragg condition is used:

$$n\lambda = 2dsin\theta \tag{2.2}$$

where n is the order of diffraction, λ is the wavelength of the X-ray, d is the inter-planar spacing and θ is the angle of diffraction. When integer values of n are satisfied for specific

λ, θ and d, then constructive interference occurs (see fig. 2.3 b) and hence reflection of the X-rays. The specificity of certain values of λ is important, as this condition only allows photons of certain energy to be reflected - exactly what is needed for a monochromatic source. Therefore, by 'filtering' the X-rays as above, the spread of energy from Al X-ray sources is reduced to $\sim$ 0.2 eV.

With the basic theory of XPS covered, one question remains unanswered - why use XPS in this experiment? Simply, XPS is a 'surface-sensitive' investigative technique, and it is the surface of the quasicrystals that are of interest - catalytic activity is generally a surface-dependent process. Incident X-rays can often penetrate micrometers below the surface of a sample - exciting the electrons that are technically part of the 'bulk' of the sample. However, these photoelectrons have a mean free path (i.e. average distance travelled between collisions, dependent on their K.E.) of $\sim$ 10 nm - meaning that the majority of their kinetic energy is lost before they can leave the sample.

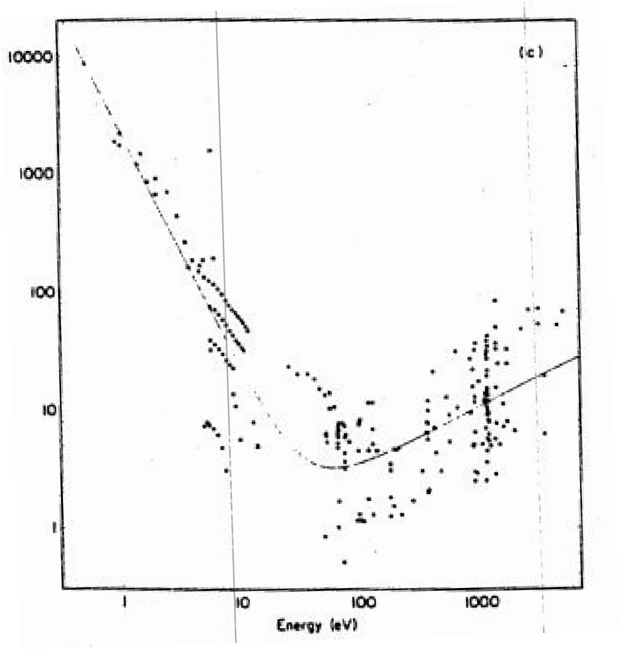

Figure 2.4: The MFP (y-axis) dependency on kinetic energy [18].

This is not the case for electrons that are excited within the first few 10's of nanometres (the surface) of the sample - they have enough kinetic energy to escape and be recorded, hence, XPS is surface sensitive.

Following the definition and justification of using XPS for this experiment, the environment under which data acquisition shall occur will be discussed; Ultra High Vacuum.

2.2 Ultra High Vacuum (UHV)

Although not a universal requirement for surface science analysis (unnecessary for Scanning Tunnelling Microscopy, Fourier Transform Infrared etc.), undertaking experiments under Ultra High Vacuum (UHV) has long been the preferred choice for materials analyses, due to the advantages it presents. For XPS analysis (and any other analytical method dependent on beams of particles/high energy radiation) however, UHV conditions are an absolute must [19]. As such, the advantages and necessity of UHV conditions for this experiment will be discussed within this section to express its importance.

Ultra High Vacuum describes a system (usually contained within a non-magnetic stainless steel chamber) that approaches $\leq 10^{-10}$ mbar of pressure. These systems are reduced to such pressures so that the beams/particles generated for analysing a surface may travel undisturbed until incident upon said surface. Take, for example, a non-ideal chamber, that is *not* in UHV conditions (i.e. standard ambient pressure) - such a chamber contains and is exposed to a large amount of residual gases (e.g. air). A clean, uncontaminated sample is placed within the chamber for analysis. Instantly, this sample is subject to a certain flux of molecules from the residual gases, sticking to or bouncing off its surface: contamination. The flux (number of molecules per unit area per unit time) of these gases striking the surface can be calculated via the kinetic theory of gases, and is known as Z, given by the Herz-Knudsen relation [20]:

$$Z = \frac{Nc}{4V} \tag{2.3}$$

where N/V is the number of molecules per unit volume, and c is the average speed of the molecules. For a gas of molecular weight M at temperature T, c is given by:

$$c = \sqrt{\frac{8RT}{\pi M}} \tag{2.4}$$

where R is the gas constant. Combining (2.3) with (2.4) and using both the ideal gas equation $PV{=}nRT$ and the relation $N{=}nN_A$:

$$Z = \frac{nN_A\sqrt{8RT/\pi M}}{4nRT} \qquad \rightarrow \qquad Z = \frac{N_A P}{\sqrt{2\pi MRT}} \tag{2.5}$$

As can be seen by relation (2.5), the flux is dependent on the pressure, temperature and molecular weight of the gas involved in the system. Assuming our non-ideal chamber is at standard ambient pressure (0.987 bar), standard ambient temperature (300K) and contains solely nitrogen (air is 78% nitrogen), the flux striking the surface of our sample is $Z = 2.91 \,\mathrm{x}\, 10^{27}$ $\mathrm{m}^{-2}\mathrm{s}^{-1}$ [19]. Presuming a standard surface atomic density of the order $\sim$ 10^{19} atoms m^{-2}, this results in a surface atom being struck by approximately 10^8 nitrogen molecules every second - or a monolayer of nitrogen is formed every 3ns. Clearly, when wishing to investigate a surface of interest it is advantageous for it to not be covered by layers of contamination almost instantaneously. Calculating for UHV conditions with pressure at 10^{-10} mbar (mbar are units used commonly in UHV related physics) with otherwise identical conditions, we find $Z = 9.09 \,\mathrm{x}\, 10^{14}$ $\mathrm{m}^{-2}\mathrm{s}^{-1}$, or rather a surface atom is struck, on average, every 20 hours. When acquiring data from a sample, a 20 hour time window is more than adequate; not only do UHV conditions prevent contamination of the sample, they provide a realistic timeframe to conduct analysis.

In addition to the necessities stated previously, UHV conditions provide a further advantage for the study of a surface - collision free recorded spectra. Section **1.2** detailed the theory of XPS - a form of spectroscopy that is dependent on the photoelectrons emitted from a sample. These emitted photoelectrons travel an average distance before colliding with other particles within a gas phase the mean free path (MFP). For a reliable recording and hence high resolution of spectra, these photoelectrons need to travel from the sample to the detector unimpeded i.e. have a large MFP. The MFP can be calculated by:

$$\lambda = \frac{k_B T}{\sqrt{2} P \sigma} \tag{2.6}$$

where k_B is Boltzmann's constant and σ is the collision cross section (probability of collision). It becomes very clear by studying (2.6) that as pressure is decreased, MFP increases - at 10^{-10} mbar the MFP is $\sim 5 \,\mathrm{x}\, 10^5$ m. This collision free environment provides a reliable recording of any photoelectrons emitted from the surface of a sample. Thus, UHV conditions have been shown to be necessary to facilitate reliable measurements for the recording of XPS spectra.

2.3 CasaXPS and Analysis Techniques

CasaXPS, as the name suggests, is a processing software tool used for the analysis of XPS data (and other spectroscopic data) that provides the user with a range of powerful analytical techniques. The discussion of the use and efficacy of CasaXPS is important, as there are a number of factors which affect the results it produces, as well as the precision with which it can produce these results. For this thesis, CasaXPS will be used for elemental peak position identification and surface composition quantification; both are commonplace analytical techniques that can provide important information about the surface under scrutiny.

As previously discussed, peak positions of an element have characteristic binding energies - electrons with equal n, ℓ but different j quantum numbers have slightly different B.E's ($\sim$ 5 eV), whereas electrons with differnet n numbers often have differences of 100's of eVs. The number and choice of peaks that can be analysed, therefore, is an advantage when dealing with intermetallic samples that often have crossover peaks for specific photoelectrons - for example, the Cu3p peak region (Cu3p$_{1/2}$, Cu3p$_{3/2}$) overlapping with the Al2p peak, or the O1s peak overlapping the Pd3p$_{3/2}$. Therefore, selection of appropriate peaks is important for both identification and quantification. Recommendations for the order of priority for analysis of peaks exist both in scientific literature and XPS-dedicated websites; however, the rule of thumb is that the most intense peak for the element is assessed. Peak position analysis using CasaXPS is the simplest function the software offers - a simple point-and-click tool allows a user with basic knowledge of the physical processes involved find and identify peaks with ease. Details of how peak position analysis will be used in this thesis are covered in section **2.5**.

Surface composition quantification is the process of analysing the area or intensity of a specific peak of an element, and comparing said area/intensity to other elements in the sample. By doing so, a percentage atomic concentration of the surface can be calculated; for example: $Al_{63}Cu_{24}Fe_{13}$, where subscripts indicate how much of the surface (as a percentage) is comprised of each element. Compositional analysis is a more advanced technique than that of peak position analysis, as more complicated physical and theoretical processes need to be taken into account. The percentage concentration of an element i can be calculated by:

$$n_i = \frac{{}^{I_i}\!/_{s_i}}{\sum {}^{I_i}\!/_{s_i}} \tag{2.7}$$

where I_i is the intensity or area of a specific peak belonging to element i, and s_i is a sensitivity factor, defined as:

$$s_i = \sigma_i \lambda_i \tag{2.8}$$

where σ_i is the Scofield Relative Sensitivity Factor (RSF) of element i, and λ_i is the mean free path of an electron from element i, with kinetic energy KE (Note: there is a parameter omitted from the denominator in (2.7) that accounts for instrumental factors. As its value is constant for all data analysed, it has been left out). The mean free path of an electron has been explained previously, but the RSF of an element needs some explanation. When quantifying XPS spectra RSF are used to scale the measured peak areas, so that changes in the peak areas represent the amount of material in the sample surface [17]. There are total RSF values for total peak regions (e.g. 2p) that are then split for multiplet states (e.g $2p_{1/2}$, $2p_{3/2}$), so that - for example - in the event that a $2p_{1/2}$ peak of an element of interest is in any way compromised (perhaps by elemental overlap), there are always other peaks that can reliably represent the amount of said element in the surface. So, for example, the Al percentage in the surface of the Al-Cu-Fe QC would be calculated by:

$$n_{Al} = \frac{{}^{I_{Al}}\!/_{s_{Al}}}{{}^{I_{Al}}\!/_{s_{Al}} + {}^{I_{Cu}}\!/_{s_{Cu}} + {}^{I_{Fe}}\!/_{s_{Fe}}} \tag{2.9}$$

s_i is a value that can be calculated simply (although calculating the MFP for complex metallic alloys is difficult, so values used will be approximate). Databases can be used to find the RSF (one such database is contained within CasaXPS), and the MFP can be calculated using a Java applet featuring modelling functions found in S. Tanuma *et al.*'s article: 'Calculations of electron inelastic mean free paths' [21]. Calculating s_i, therefore, is a simple, quick process. However, finding the area I_i of the peak is a decidedly more tricky procedure.

CasaXPS cannot be used as a black box tool with XPS data; you cannot simply point at a peak corresponding to the B.E. of a known element and say the area underneath it is is 100% Al. Surface composition calculation would be inaccurate for one, but to do this is to ignore several basic physical aspects that can affect the analysis being undertaken. Take, for example, an Al-Cu-Fe QC. All 3 metals interact with oxygen to varying degrees (strongest to weakest being Al, then Fe, then Cu), forming 'native' oxides - Al_2O_3, Fe_2O_3 and CuO. If this QC has been exposed to air, these oxides will form on the surface almost instantaneously (chemisorption), as well as carbon based organic bonds (C-O for example, physisorption). The chemisorption processes will shift the binding energies that we expect from the elemental peaks as the bonds are altered from a pure state to an oxide

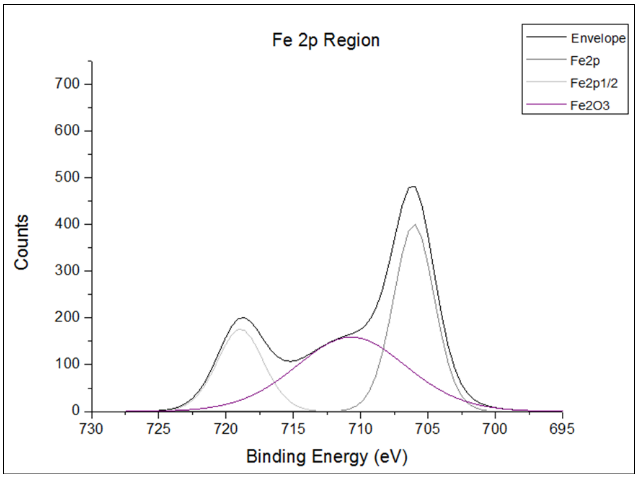

Figure 2.5: An example of peak curve fitting.

state - additionally, these peaks may be broadened, covering a wider range of energy. The broadening and shift of a peak can be analysed using a process known as 'peak curve fitting' within CasaXPS. Peak curve fitting is a theoretical method that has been described as 'equal parts science, art and luck' that certainly becomes a more useful tool as experience using it increases. The basis of the method is the premise that any shape of peak can be created using a series of smaller peaks that obey Gaussian/Lorentzian statistics. A 'background data' curve is added that simulates the background data that 'would' be there, had no peak been measured which is also dependent on mathematical models. For all curves fitted in this thesis, the background models used are either 'Shirley' or 'Tougaard'. The Shirley algorithm attempts to use information about the spectrum to construct a background that is sensitive to changes in the data, whilst Tougaard is based on the idea that an electron emitted loses energy and appears as a contribution to the background noise. An example from data analysed in section **3.1** is shown in fig. 2.5 (raw data has been omitted for the purpose of this explanation). As can be seen, there are 3 peaks that make up an overall envelope - Fe2p, Fe2p$_{1/2}$ and what could be Fe_2O_3 (later proved incorrect). The aim of peak fitting is to fit this envelope with the raw data that is taken from the data collection instruments. For relatively simple peaks such as fig. 2.5, previous knowledge of the sample - it contains Fe - and Fe's native oxide binding energy, means peak fitting is an easy process. Difficulties arise when unknown quantities appear, or peaks overlap between elements of interest (i.e. Pd and O, as discussed in section **3.2**). An important point to note is that, just because an oddly shaped peak *can* be explained by fitting 8 smaller peaks, doesn't mean it *should* be. As the peak fitting function depends on mathematical quantities, theoretically, any shape can be explained if enough Gaussian/Lorentzian variables are created. Thus, logical thinking backed by scientific knowledge of the sample and its oxides (or carbides etc.) is a must when using peak fitting analysis.

The physisorbed species can be analysed to find (in the case of methanol deposition) what sort of organic structures are formed i.e. C-O, C=O etc. Analysing these structures will give an insight into how the surface reacts with the methanol; the type of bonds that are made with the surface will indicate how the methanol decomposes, giving an insight into why this reaction occurs.

One final aspect that should be considered when analysing XPS data is the natural shape and area of the elemental peaks. First, the effect of multiplet level splitting shall be considered; as previously discussed, core levels can be split into multi-level components ($2p_{1/2}$ etc.). The splitting phenomena is evidenced within the spectra by the ratio of the area of the peaks that arise from the region that is split, as shown in tab. 2.1.

Subshell	j values	Ratio
s	1/2	n/a
p	1/2, 3/2	1:2
d	3/2, 5/2	2:3
f	5/2, 7/2	3:4

Table 2.1: Ratio table that defines the area of the split level peaks.

Thus, when analysing the peaks it is important to keep this rule in mind. This rule equally applies to RSF values - with the RSF values for $2p_{1/2}$ and $2p_{3/2}$ summing to give an overall value for the 2p region.

It can be easy to assume that electrons that are excited from an element are done so in a uniform manner i.e. the peak formed is symmetrical in shape. However, metallic elements are known to exhibit asymmetrical peak shape - a phenomenon that can be explained by an in-depth physical appreciation of the photon-absorbing nature of XPS. Instead of the simple ‘one photon, one electron’ theory that is adequate to describe the basis of XPS experimentation, the reality is slightly more complex. When a photon is absorbed by a material, the energy that is transferred can not only excite the electron, but can cause ‘plasmonic excitations’ at the surface as well. A plasmon is a collective oscillation of free electrons, hence, such asymmetric peaks do not appear from insulating elements. The consequence of this behaviour will be discussed more prominently within the discussion chapter.

As the theoretical and analytical aspect of the experiment has been explored, the physical and experimental side shall now be explained.

2.4 UHV Preparation and Instrumentation

As previously discussed within section **2.2**, UHV conditions are a must for XPS studies. Contained within this section is the procedure for bringing a UHV chamber down to adequate pressure conditions, as well as how a sample is taken from the laboratory and moved into an analysis chamber. There are a number of books, manuals and other literature that can give an overview of each characteristic of UHV technology (particularly useful is ‘A User’s Guide to Vacuum Technology’ [22]), however, only the aspects which are relevant to this experiment will be discussed.

To bring a chamber into UHV conditions, first, a series of ‘pumps’ are used to evacuate any air or gas that is contained within the chamber. Vacuum pumps can be split into 3 rough groups [15]:

- Displacement pumps
- Momentum transfer pumps
- Entrapment pumps

A schematic of these pumps gives an indication of how they are used - fig. 2.6:

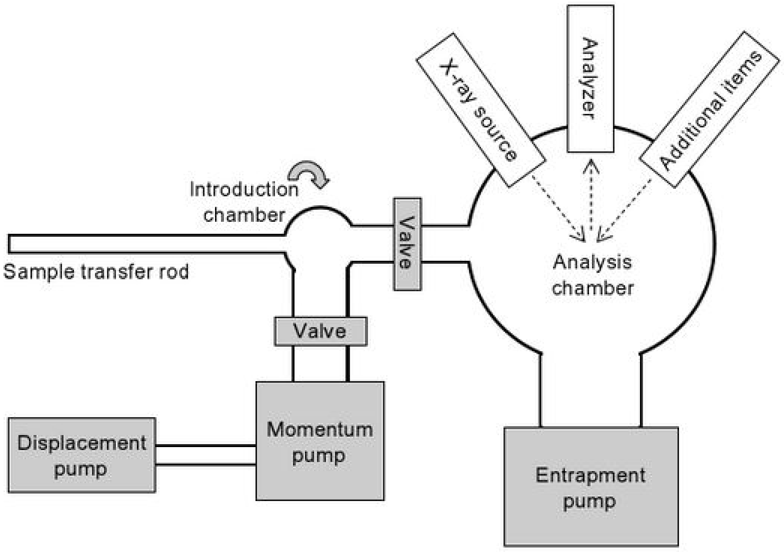

Figure 2.6: A schematic of a rough UHV setup [15].

If a chamber is at ambient pressure, the first pump that needs to be used is a 'Displacement' pump, as this brings the pressure down to ∼10^{-4} mbar (ideally, but in practice ∼10^{-2} mbar) - a pressure necessary for the next pump to begin working at. An example of a displacement pump (and indeed, used in this experiment) is a rotary pump; a schematic of which has been included within the appendix (5.3). The basic premise of such a pump is that gas from the chamber enters a suction chamber within the pump, which is compressed by a rotor and vane and then expelled to the atmosphere through a discharge valve [22]. By running this pump for a certain amount of time, the chamber will be evacuated down to pressures that are suitable for a 'Momentum' pump to commence pumping. These pumps cannot evacuate a chamber from atmospheric pressure - they can only operate once the turbo pump has reached ∼10^{-4} mbar. A turbomolecular pump is an example of such a pump - it reduces the pressure still further down to ∼10^{-7} mbar (∼10^{-10} mbar depending on the size of the chamber). A turbomolecular pump can be described as a high-speed molecular baseball bat; it is a turbine that compresses gas by the transfer of momentum from the high speed rotating blades to gas molecules [22]. The pump consists of slotted rotating blades and slotted stator (stationary) blades - the relative velocity of the blades to each other makes it likely that a gas molecule from a UHV chamber is transported from the gas inlet to the gas outlet of the pump. Again, a schematic of the turbomolecular pump is contained within the appendix (5.3). Finally, the 'Entrapment' pump, or more specifically, an ion pump. These pumps are self-contained and can reach UHV pressures with back pumping in series, unlike turbo pumps; the technique in which pressure is reduced can be damaging to samples, so the previous pumps are a necessity. An ion pump

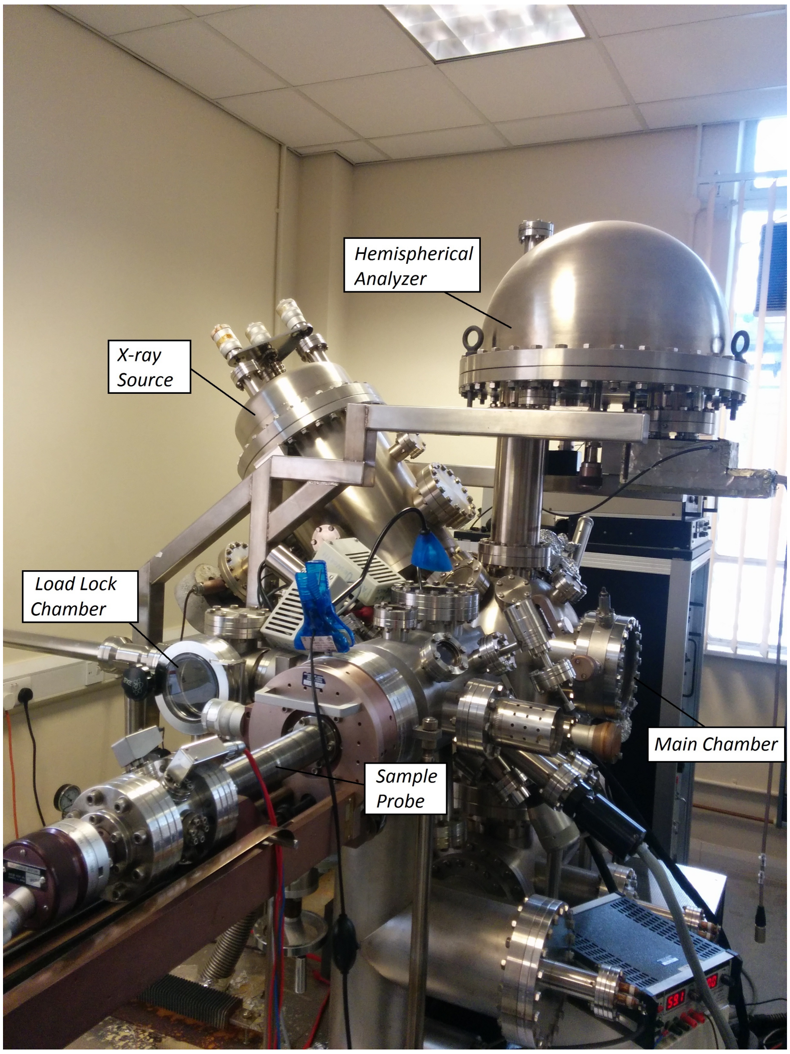

Figure 2.7: The UHV setup used to conduct the experiment.

is less mechanical than the previous pumping methods: an electric discharge ionizes gases within the chamber, which are then attracted and accelerated towards a potential where they are captured on a Ti film - removing them from the chamber.

Once the system has reached 10^{-7} mbar, it needs to be 'baked out'. This involves covering the entire system in heat-proof modules and slowly heating every component $\sim$ 100-200 degrees above room temperature. This desorbs any rest gas (comprised mainly of water) in the system that would inhibit reaching UHV pressures (as water vapour pressure is too high). So, to conduct analysis on a sample, it needs to be placed within the main chamber. At atmospheric pressure, the sample is placed within an 'load lock' chamber (see fig. 2.6) and attached to a magnetic sample holder as shown in fig. 2.6. This chamber is then evacuated using the pumps as described. When the pressure in the load lock has reached high vacuum, a valve can then be slowly opened between the load lock and the main chamber that allows an equalisation of pressure between the two chambers. The magnetic sample holder is then moved into the main chamber using a probe - at this point another probe is attached to the sample holder and the original is retracted. The main chamber is closed off and then evacuated once again. Once UHV pressures are reached,

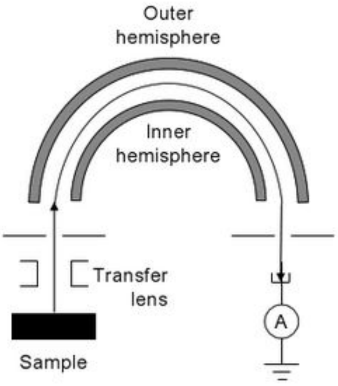

Figure 2.8: Schematic of the CHA. The electrons are focussed by the transfer lens and passed through the gap between the two hemispheres. The CHA can be used in two separate modes - survey scan or high resolution peak focussing.

the sample can be analysed. The theory of how XPS data is generated has been covered within section **2.1**; the collection of this data will now be discussed.

When performing XPS scans, it is important to have a high resolution energy analyser: it allows for closely separated peak identification. Used in most modern XPS instrumentation, a Concentric Hemispherical Analyser (CHA fig. 2.8) provides energy resolution down to 0.01 eV - higher resolution than the X-ray source energy spread! This means that the resolution of an XPS peak is primarily dependent on the X-ray source, not the analyser [15]. The CHA is as described - 2 concentric hemispheres (one inside the other) with radii R_{in} and R_{out}, operating in one of two modes: Fixed Retard Ratio (FRR) or Fixed Analyser Transmission (FAT). FRR mode consists of applying a specific potential to these hemispheres, resulting in electrons of specific kinetic energy being allowed to hit the detector. The potentials are as follows [15]:

$$V_{in} = E_0[3 - 2\frac{R_{cl}}{R_{in}}], \qquad V_{out} = E_0[3 - 2\frac{R_{cl}}{R_{out}}] \tag{2.10}$$

where E_0 is the desired energy to be detected and R_{cl} is the average of the two radii.

Thus, E_0 can be 'swept' from 0 eV to the maximum X-ray source energy, providing a survey scan (scanning the sample over the total energy range the X-rays can excite).

FAT mode provides a high resolution 'zoomed-in' scan of a specific range of kinetic energy to allow a closer look at one peak or set of peaks. FAT mode is achieved by keeping E_0 at a constant value by varying the voltage applied across the lens - meaning that again, the resolution is independent of the K.E of the electrons. The resolution can thus be given in units of E_0 - known as the pass energy. This mode gives a much higher resolution compared to FRR, but at the expense of sensitivity.

Following on from the instrumentation of the experiment, the procedure of scanning the sample(s) will now be considered.

2.5 Scanning samples

Previous studies on Al based QCs as catalysts have used crushed powdered versions of the sample. Quasicrystals by nature are brittle materials, allowing them to be crushed into a powder effectively; the crushing of the samples creates a greater surface area for the interaction between the catalyst and the reactants. However, the crushing of a sample makes surface science studies troublesome - a powdered surface has many random orientations, making it difficult to assess on an atomic level. Combined with the complexities of quasicrystalline structure, this means that instead of a powdered sample, model samples will be used for the following studies i.e. single grain QCs with well understood surfaces [10].

The ‘log’ of events for the initial studies for each QC is as follows:

Al-Cu-Fe

Step	Procedure
1	Dirty sample survey scan
2	30 min Ar$^+$ ion sputter
3	Survey scan Cu2p and Cu Auger at 50 eV pass Fe2p and Fe Auger at 50 eV pass
4	Survey scan after 24 hrs
5	45 min Ar$^+$ ion sputter Survey scan Cu, Fe2p and Fe Auger region at 50eV Fe 3s, Cu 3p at 50eV pass Another survey scan after 45 mins
6	45 min Ar$^+$ ion sputter after 24 hrs Survey scan

Al-Pd-Mn

Step	Procedure
1	Dirty survey scan
2	50 min Ar$^+$ ion sputter Survey scan Pd3d, Mn2p regions at 20 eV pass
3	Survey scan after 24 hrs Al2p region
4	Survey scan after 48 hrs 50 min Ar$^+$ ion sputter Pd Auger region Test scan [1] 55 min Ar$^+$ ion sputter Survey scan
5	Survey scan after 24 hrs
6	Survey scan after 48 hrs
7	55 min Ar$^+$ ion sputter Mn Auger region Survey scan
8	Survey scan after 24 hrs
9	Sample plate scan [2]

Table 2.2: The two procedures outlined for the initial studies on peak positions and surface composition. [1-2] Will be explained within the discussion chapter.

Tab. 2.2 presents an overview of the first steps taken to acquire the data that is used within the results chapter. Note: this is just a general overview of the steps required to prepare a sample and declare it ’clean’ i.e. sputter for an amount of time, scan, repeat etc. The full log of procedures that were performed will be contained within the appendix (5.4).

The initial studies that will be undertaken with each quasicrystal are as follows: using XPS, the exposed ‘dirty’ surfaces will be scanned. Following from this, each QC will be sputtered with Ar$^+$ gas and scanned again. Sputtering is the process of firing an inert gas at the sample, with the aim of knocking off any impurities (in the form of oxides, organic carbides etc.). However, if the kinetic energy of the sputter gas molecules is too high, or a sample is sputtered for too long, then the surface can become damaged or pitted. By creating a rough surface, it is theorised that the methanol is more likely to ‘stick’ to the surface and decompose. However, in sputtering QCs, some elements are removed preferentially (for Al-Cu-Fe, Al-Pd-Mn, Al is sputtered away due to its lower mass) which changes the surface composition. QC composition is a finely tuned quantity, and if it is changed then the QC structure at the surface will be destroyed, leaving a different phase. Finally, the sample will be annealed and scanned again. Annealing is the process of heating up the QC close to its melting point, so that quasicrystalline structure in the surface can be restored by returning the QC to its original composition and 'smoothing out' defects. The aim of these initial scans is to study the effect of the sputtering and annealing processes on the quasicrystal surfaces.

The dirty samples will have been exposed to air, so natural oxides are formed. The dirty sample scans will be used to look at the effect the formation of these oxides has on the binding energy peak positions of the metals within the QCs (known as chemical charge shifts). To accomplish this, the peak positions measured will be compared to values found in scientific literature: this will allow the identification of what *type* of oxide is found (i.e AlO or Al_2O_3 etc.). The peak positions will continue to be analysed as the sample is sputtered and annealed. Again, this is to study what effect these processes have on the sample surface. In addition to this, the composition percentage of the surface as it undergoes these processes will be studied; the calculations of which are as detailed within the previous section. This is to further understand the effect sputtering and annealing (particularly sputtering) has upon the QCs - for example, is one metal preferentially sputtered away from the surface?

Annealing the samples is a simple process - the samples are heated to a specific temperature that can be controlled via an applied current. The heating of the samples smooths out the surface and helps to reduce any defects which may form. For Scanning Tunnelling Microscopy (STM) experiments, for example, annealing can be performed over a large timeframe, providing an 'atomically flat' surface - perfect for surface images. However, atomically flat surfaces are not a necessity for XPS experiments; the annealing that takes place in this experiment was conducted for 2-3 hrs at a time at 650 °C until QC composition and structure at the surface are reached.

So, in summary, the steps taken before data acquisition and attempted methanol deposition follow a simple cycle - sputter for $\sim$1 hr (repeated until a the QC is 'clean'), then anneal for 2-3 hrs.

2.6 Deposition

The crux of the experiment is studying the way in which methanol decomposes at the surface of the aforementioned quasicrystals, so the deposition of methanol is obviously an important step. A major issue for introducing a 'foreign' material into a UHV chamber is that it has to be as close to 100% purity as possible - any contaminants within the methanol could potentially negatively affect the way in which the quasicrystals react. Thus, purification, or, in this case, distillation, of methanol is an important step pre-deposition. Distillation is a process in which a liquid that is composed of a mixture of liquid and vapour is selectively evaporated/condensed so that its constituents are separated out. Applying this process to the methanol allows any contaminants to be removed - purifying it.

To distil the methanol, a variation of a cold trap will be used. Cold traps are frequently used for the separation of condensable components from mixtures of gases and vapours [23]. The basic premise is that, when submerging a vessel containing a mixture of a liquid and a vapour into a very cold atmosphere, the liquid will freeze - allowing the vapour to be removed and condensed. To provide the cold temperatures, containers with dry ice or (more commonly) liquid nitrogen are used. By submerging a suitable vessel containing methanol in a bath of liquid nitrogen, any contaminants can be removed by attaching this vessel to a vacuum system and pumping away the unwanted material.

Following the purification of the methanol (this process may be repeated a number of times), it can then be deposited onto the sample. By ensuring that the 'pipeline' i.e. the tube that contains the methanol is thin, the methanol can be treated as a beam that can be directed at the sample when in the main UHV chamber - allowing deposition and, hopefully, decomposition at the surface.

The following chapter presents and details the results collected according to the methods outlined within this chapter, as well as providing a discussion that explains these results, as well as rationalising and justifying the assumptions made about said results.

Chapter 3

Results and Discussion

Presented here are the results from each step of the experiment - for both quasicrystals (Al-Cu-Fe, Al-Pd-Mn) at the dirty, sputtered and annealed stages. The presented results will be summarised briefly upon presentation, with a further discussion in a separate sub-section.

3.1 Al-Cu-Fe Results

The results obtained for the Al-Cu-Fe QC are presented here, with a table of peak positions, survey and core level spectra and compositional calculations highlighting the following observations made from the data. The exposed sample exhibited carbon and oxygen contamination at the surface, which led to the identification of Al_2O_3 and carbon physisorbed species due to their respective binding energies. Subsequent sputtering removed these features, as evidenced by binding energy shifts and the disappearance of the carbon core level. The interference of the Cu3p peak made peak analysis and compositional calculations difficult, resulting in an arduous acquisition these values. However, compositional analysis using the Al2s core level returned results expected from literature, and highlighted a segregation layer of Al which affected peak acquisition [38].

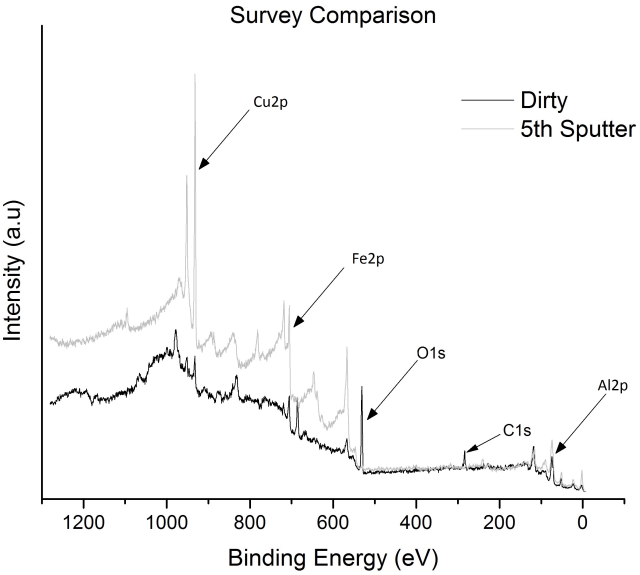

Figure 3.1: A survey comparison between the dirty scan and final sputter scan of the Al-Cu-Fe quasicrystal.

Fig. 3.1 highlights the stark difference between the dirty and sputtered scans. Here, it is clear that peaks are shifted en masse, and that the intensity of the elements are greatly multiplied. The presence of oxygen and carbon are removed (as labelled). Relating back to the Al2p issue briefly, it is worth noting the intensities of the two scans towards the end of the chart - they are roughly equal. This highlights the difficulties of exciting the Al in the QC adequately with the radiation source used, as the peaks generated are small, and can get dwarfed by surrounding peaks and noise. This survey intends to give an overall picture of the Al-Cu-Fe sample, with all the relevant peaks that have been measured highlighted. The set of figures presented within this chapter will explore these regions with more depth, allowing particularly interesting features to be analysed in a more meaningful manner.

The following table presents the dirty and sputter data for the Al-Cu-Fe quasicrystal core level and Auger electrons, recorded as stipulated by tab. 2.2. The uncertainty placed upon each value is estimated to be 0.1-0.2 eV [10]:

	Binding Energy (eV)						Auger	K. E. (eV)
	Cu2p	Fe2p	Al2p	Oxides	CuO	Al$_2$O$_3$		Cu LMM
Elemental	932.5[24]	706.5[25]	72.8[26]		529-530[27]	531.1[27]		918.6[28]
Step								
1	932.4	706.0	74.2		n/a	531.1		919.6
2	932.3	705.9	73.6		n/a	530.7		919.5
3	932.3	706.0	73.6		530.7	532.0		919.6
4	932.5	706.0	71.6		n/a	n/a		919.4
5	932.3	706.1	73.0		530.4	531.9		919.5
6	932.1	705.3	73.8		n/a	n/a		919.6

Table 3.1: The peak positions of the 2p regions for each element in the Al-Cu-Fe quasicrystal, from as received (dirty, step 1) and each subsequent sputter (step 2-6).

Note: in this incidence '2p' is a general name for the Cu2p$_{3/2}$, Fe2p$_{3/2}$ peaks. The resolution of the scans at the Al2p binding energy value cannot distinguish between the Al2p$_{1/2}$ and Al2p$_{3/2}$ peaks; it is an abbreviation for easier comparison. However, the previous multiplet rule of splitting RSF values (section **2.3**) is still taken into account for each peak/region. The dirty sample showed clear signs of oxidation, both in an oxygen peak and the shifted values for the 2p regions (particularly Al). The vacuum reached for these results to be taken was not ideal (10^{-10} mbar), reaching only 3^{-9} mbar - which explains the re-emergence of the presence of oxygen when the sample is left in the chamber for any extended period of time.

The justification of specifying the oxides formed come from comparisons of peak positions within the specified citations. These oxides can be further confirmed by the comparison of each region's 'shape' that is formed under oxidation. Presented here, therefore, are a series of graphs that show evidence of the presence of oxidized species of Al, Cu and Fe.

Fig. 3.2 shows the dirty sample scan Cu2p core levels that has been compared to CuO scans in scientific literature to confirm the shape and peak positions [29]. The peaks include the multiplet splitting of the 2p region, as well as the oxygen auger electron and

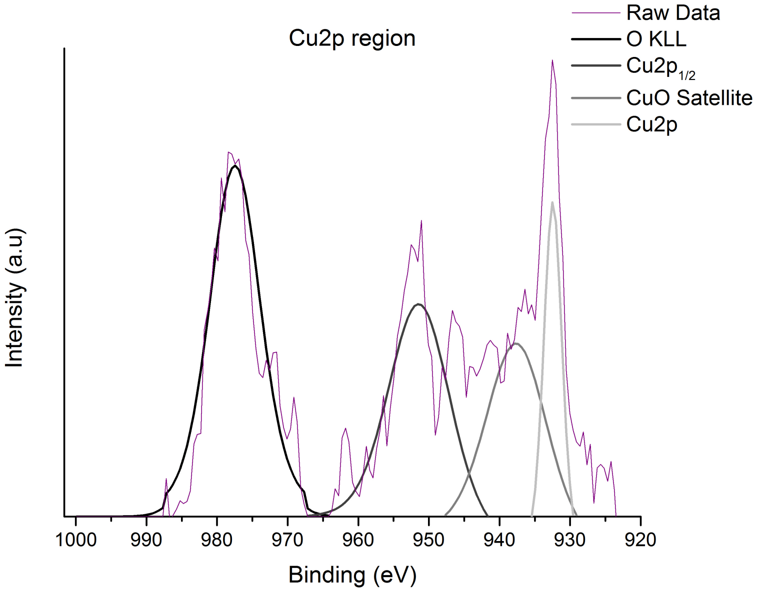

Figure 3.2: The Cu2p core level peaks as collected from the dirty Al-Cu-Fe sample using XPS, complete with fitted curves with an overlay of the raw data.

a characteristic CuO satellite. The 'satellite' peak that has been identified is the primary feature for comparison - see the appendix (5.5) for a figure from an article that corroborates the identification of fig. 3.2 as CuO [29]. When comparing with the cleanest sputtered surface (as taken from step no.4), it becomes clear that CuO is formed on the dirty sample, and has subsequently been sputtered away. The shifting of peak positions and removal of both the oxygen auger electron and CuO satellite are direct evidence of the sputtering and highlight its usefulness in cleaning the sample surface. The large intensity increase seen in fig. 3.3 is due to the segregated Al_2O_3 layer being sputtered away, hence no longer dominating the surface. This phenomenon is responsible for the increase in intensity seen in the rest of the peaks post sputtering and shall be discussed in detail in the discussion section.

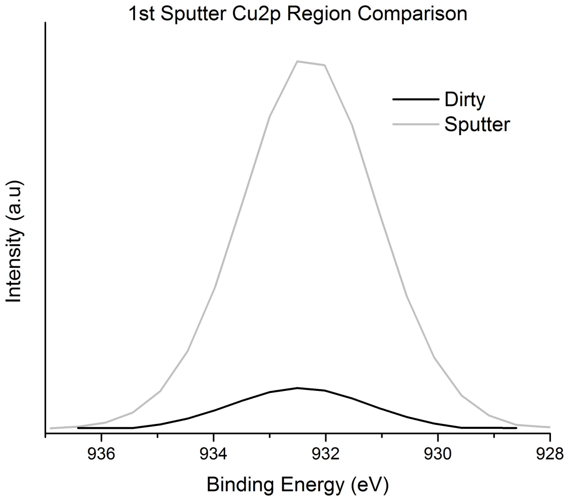

Figure 3.3: 1st Sputter Cu2p region to highlight the effect of effect of sputtering.

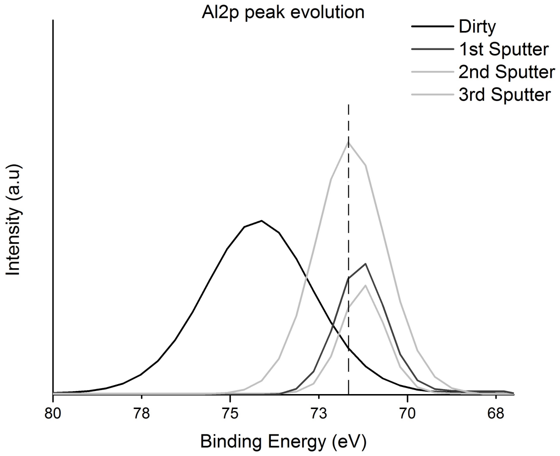

Figure 3.4: Al2p region evolution as the surface is progressively sputtered.

Perhaps a more direct way of studying the evolution of the sample surface is to compare the peak of a region as it is progressively sputtered - as seen in fig. 3.4 for Al2p (where the 4th and 5th sputters have been omitted for clarity on the plot). The difficulty in capturing the Al2p region has previously been discussed (and shall be discussed further), but what is presented are the curves fitted under the region that correspond to Al2p's B.E. The markedly large shift of the Al2p peak between dirty and sputtered samples is plain to see and re-affirms the presence of the native Al oxide Al_2O_3 - the binding energy of which is 74.6 eV[27]. The large intensity difference as highlighted on the 2nd sputter is due to oxide formation and overlap - again discussed within the next section.

The Fe2p region presents difficulty for analysis - the asymmetric shape of the elemental peaks are difficult for a beginner's use of CasaXPS (especially when trying to avoid overuse of the mathematically driven aspect of curve fitting), which affects the confidence of the identification of oxides and compositional calculations. However, the evolution of the Fe2p region is presented in an attempt to highlight the changes that occur upon cleaning the sample i.e. when the signal to noise ratio increases:

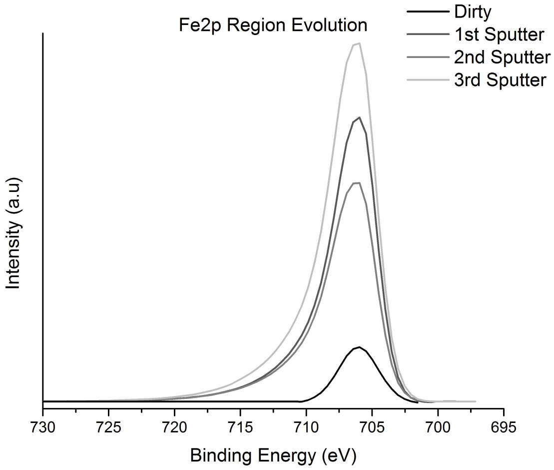

Figure 3.5: Fe2p region evolution to highlight the effects of cleaning a sample.

To conclude the group of oxidation evidence, a series of graphs that focus on the oxygen region are presented:

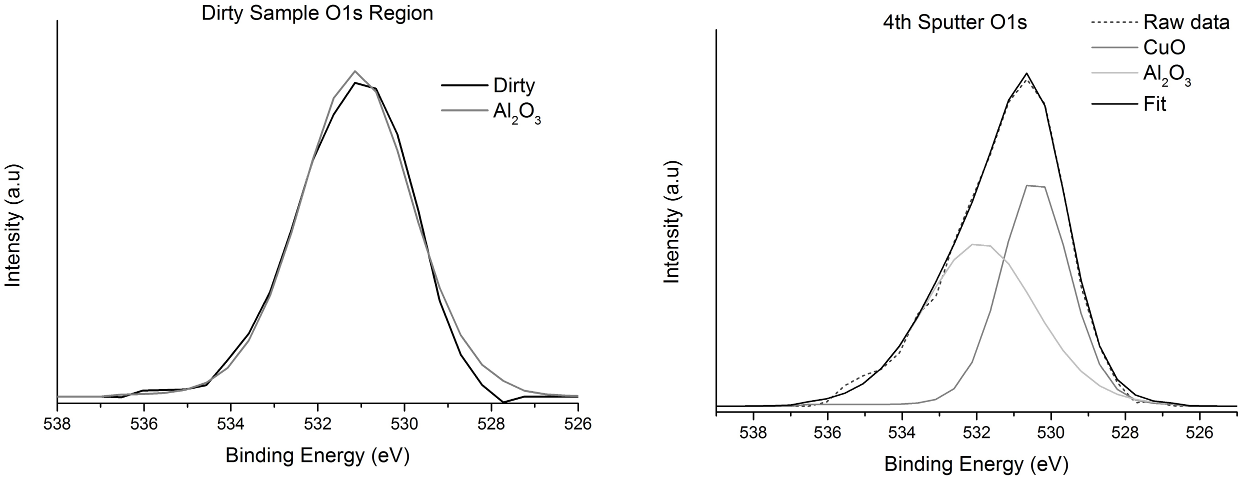

(a) Dirty oxygen region.

(b) 4th sputter oxygen region.

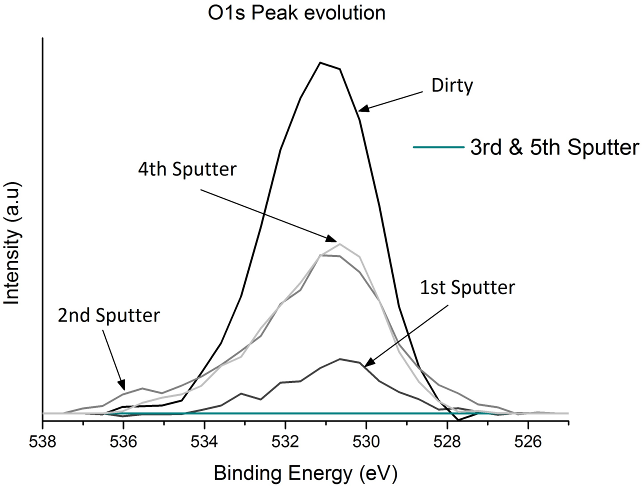

(c) Oxygen evolution graph that shows the reduction of oxygen over the 6 scans performed.

Figure 3.6: The presence of oxygen as detected over all 6 scans performed for Al-Cu-Fe. Fig. a) demonstrates the presence of oxygen that has been attributed to Al's native oxide. b) shows the detection of a second oxide that has been tentatively identified as CuO. c) shows an overall reduction in the oxygen presence.

Fig. 3.6 shows a collection of graphs that give testament to the presence (and subsequent reduction) of oxygen on the surface of the Al-Cu-Fe sample. Note the necessity for 2 curves used for fitting to the data in fig. 3.6b, resulting in the suggestion of detection of 2 oxides. CuO has been tentatively identified as the second oxide, as the peak position shift combined with the comparison of the CuO satellite feature in oxidised scans give weight to this argument. However, the B.E. value that has been ascribed to CuO could also be due to C=O - a possibility that also has evidence behind it due to the appearance of C and the identification of C=O on the dirty scan. This quandary will be dealt with in more detail within the discussion chapter.

As well as the oxidation of the sample, a carbon contamination was prevalent in the dirty sample survey scan. Although not particularly relevant to the Al-Cu-Fe section of this report, it is a noteworthy peak for analysis (especially for the deposition performed upon on Al-Pd-Mn, discussed later). Fig. 3.7 is the C1s peak as it appears on the dirty Al-Cu-Fe sample - showing evidence of either C-O or C=O.

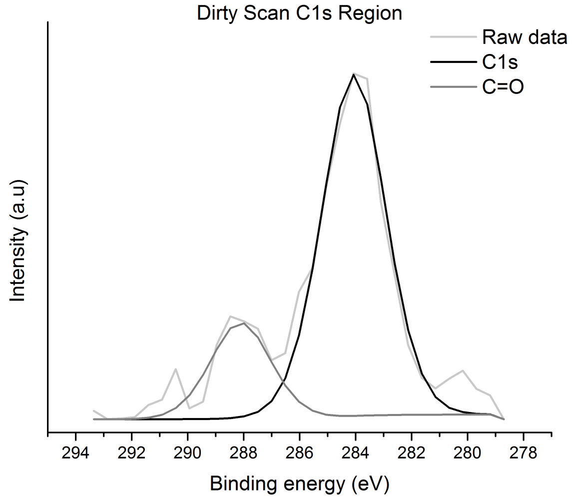

Figure 3.7: The C region as detected on the dirty sample surface.

When comparing the binding energy of C=O to that observed in fig. 3.7, it can easily be said that C=O has been detected at the surface and has subsequently been sputtered away in later scans (there is little to no suggestion of carbon in the further scans) [10]. Therefore, is the attribution of the second oxide in fig. 3.6b to CuO incorrect, as C=O in the oxygen region has a B.E of 533eV - the same as CuO [27]? Or does the lack of C in later scans suggest that this assumption is correct, and it is just a coincidence? The matter shall again be discussed further within the discussion chapter. The smaller peak observed at 280 eV which has not been fitted can be tentatively identified as CO, carbidic carbon [30].

Finally, the compositional calculations made throughout the sputtering processes are presented:

	Composition %		
	Al2p	Cu	Fe
Step			
1	82	7	11
2	71	14	15
3	71	13	16
4	69	18	12
5	55	25	20
6	75	16	9

	Composition %		
	Al2s	Cu	Fe
Step			
1	88	5	7
2	49	24	27
3	56	20	24
4	53	28	19
5	54	25	20
6	51	31	18

Table 3.2: Calculated values for the composition of the surface of the Al-Cu-Fe quasicrystal. Composition has been calculated with both Al regions, as stated within the main text.

These values have been calculated using both the Al2p and Al2s regions, allowing a direct comparison. There is a 10% uncertainty placed upon each value calculated (discussed later). These values are comparable to the 'true' composition of the QC: $Al_{63}Fe_{24}Fe_{13}$, or, at least, within a few percentage when considering the uncertainty. Importantly, the overall concentration hierarchy (mostly) adheres to the natural composition of the QC (particularly on cleaner scans) i.e. predominately Al, with low amounts of Fe and a Cu value somewhere between the two. A graphical scheme of the compositions is presented:

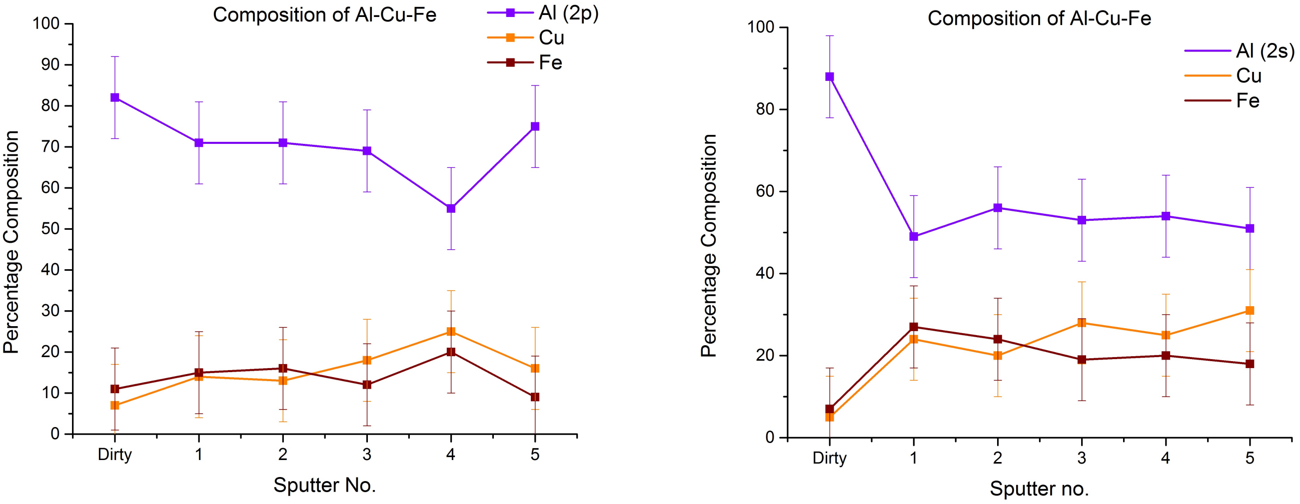

(a) Al2p Composition.

(b) Al2s Composition.

Figure 3.8: Graphical representation of tab. 3.2.

Discrepancies in this order, as well as the collection of the Al2s region will be discussed further in the following section.

3.1.1 Al-Cu-Fe Discussion

Al2p Region

Before the crux of the peak position analysis is discussed, it is worth mentioning the difficulty and nuance of analysing the Al2p region. For completeness and brevity, the peak position for Al2p was included in tab. 3.1. However, it is well known that in high Cu concentrations the Al2s region should be studied as well as or, indeed, instead of the Al2p region [27]. The reasoning behind this selective analysis is that the Cu3p region overlaps directly with the Al2p region. The binding energy of Al2p: 72.8 eV[26], for Cu3p: 75.13 eV[31] - a difference of ~3 eV. When scanning in FRR mode to collect a survey scan this difference is very difficult to detect - meaning that the Al2p, Cu3p peaks are detected as one large peak as opposed to two separate peaks. Using CasaXPS it is possible to use peak fitting to account for this effect - but it does mean that the peak position of Al2p as displayed in tab. 3.1 is dependent on the mathematics behind Gaussian/Lorentzian curves.

It is difficult, therefore, to conclusively say what is the causation behind the increasing B.E. values seen from scan no. 4 onwards for Al2p when the following is considered. The chemical shift observed for the Al2p region when Al_2O_3 has formed has been reported as:

74.2 eV[32] - a result that appears from the dirty sample scan and can be confirmed by the existence of an oxygen peak that has been shifted according to Al oxide formation [27]. By the same logic, if scan no. 4 is considered to produce the cleanest sample (no evidence of oxygen or carbon, with small/no peak shifts), then the increase in B.E. could correspond to the B.E. and re-formation of Al_2O_3 at the surface [27]. Scan no.5 seems to lend weight to this argument as it shows the re-appearance of oxygen as well as a chemical shift for Al2p moving towards Al_2O_3. Yet, scan no.5 shows no oxygen and a shift for the 'Al2p' region - a result which suggests that the Cu3p peak is starting to dominate over the Al. To further muddy the waters, the peak position for Al2s from the scan taken at the 6th sputter (116 eV) is consistent with Al_2O_3 shifted Al2s [33] - yet the scan shows no evidence of oxygen! So, to summarise: the Al2p region is either being affected by the formation of Al_2O_3, or the Al in the QC is being preferentially sputtered away from the surface which each sputter - allowing the Cu3p peak to dominate, as shown in fig. 3.9.

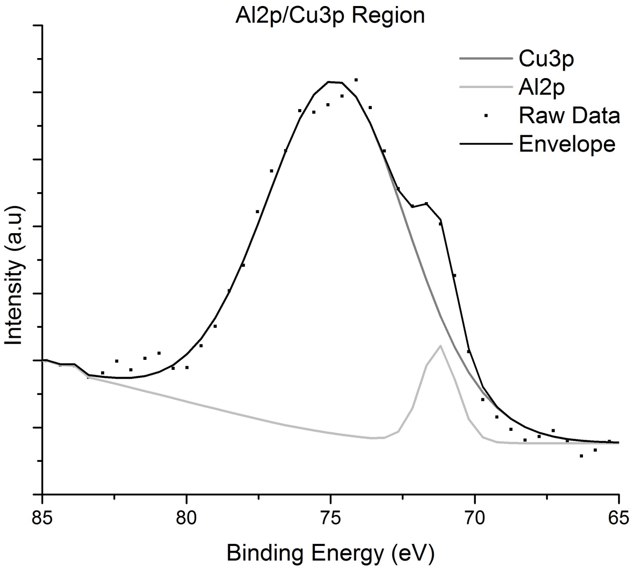

Figure 3.9: An example taken from step 3 that shows the domination Cu3p has over the Al2p region

Oxidation/Carbon Contamination

Perhaps lending weight to the aforementioned oxidation solution to the peak position shift issue is the reduction of the peak position of the Cu LMM line as the sample is sputtered. Studies that have contained analysis upon this particular Auger line agree that a K.E. shift occurs under the presence of Cu oxides, but the value of these shifts vary [34]. So, if it is assumed that some shift occurs upon Cu oxidation (as evidenced within tab. 3.1) and there is sufficient oxygen presence on the survey then, presumably, some form of Cu oxide is present on the sample. As the sample becomes cleaner (towards scan no.4) the K.E. value for Cu LMM tends towards the 'elemental' or accepted natural value and the presence of oxygen in the scans falls away. However, as the sample becomes dirty again (scans 5-6) the shifts start to increase - returning to the value obtained when scanning the dirty sample; yet, as previously discussed, no oxygen is present at scan no.6. Again, these results seem to point towards two opposing conclusions: the Cu within the QC has become oxidised and is hence shifting the recorded values - or, the shifts seen in the later scans (which show no oxygen) are in fact due to the heavy sputtering of the sample, or some unknown cause. Of the two theories, the oxidation of the surface seems to be the more likely, with the lack of oxygen peak perhaps due to other high intensity peaks ‘drowning out’ a small peak (low signal-to-noise ratio).

Another possible solution that could be considered is that CuO never actually formed at the surface (supported by the apparent formation of C=O which corresponds to similar B.E. values near the oxygen peak) and that the shifted peaks that are just caused by the sole formation of Al_2O_3. Studies upon the oxidation of both Al-Cu-Fe and Al-Pd-Mn quasicrystals have shown that for the former, the surface develops an oxidised layer that consists only of Al oxides and that neither Cu nor Fe form an oxide layer [35]. Of course, not all QC’s are alike, so direct comparison isn’t necessarily useful; however, it does serve as a point of contradiction to the CuO argument, despite the satellite feature identified on the dirty sample. Quite possibly, this feature could simply be ‘noise’ from the sample as, for dirty samples, there is a large quantity of activity that could interfere with the signals received. So, with the CuO assumption now attributed to the formation of C=O at the surface - what causes the peak Cu shifts and second peak observed ‘underneath’ the O1s peak? C is not detected on any of the sputtered scans, so the C=O has been sputtered away and, likewise, oxygen is not detected in either step 4 nor 6. As mentioned before, the shifts may be due to the formation of Cu within the Al surface structure.

A final theory for the shifted peaks seen is charge transfer - the effect changing bonds in surface structure can have on binding energies. As previously discussed, sputtering the surface of a QC sample changes its finely tuned composition - destroying the QC structure, leaving a periodic system. In this phenomena, electric charge can effectively be ‘borrowed’ from elements within the surface, to produce an overall positive or negative shift. Consider the Al2p shift seen at step 6 in tab. 3.1 - positively moved by 1 eV. The other displayed peaks (Cu2p, Fe2p) have collectivity shifted by 0.6 eV negatively away from their elemental values. It may not be unreasonable to suggest that (considering some Al oxide formation) charge transfer is to blame for the shift seen. Previous studies undertaken on a periodic $Al_{90}Cu_8Fe_2$ alloy found shifts of up to 0.2 eV - although the composition calculated for the non-periodic surface scanned in this study is some way off this composition - there is a precedent set for charge transfer in Al-Cu-Fe alloys [36].

Whatever the reason, the outcome (although mildly interesting) of the oxidation problem has no direct bearing on the study as a whole (discussed within the following subsection), and merely serves as a tool for the increasing of experience of the author in such matters.

Aside from this problem, the oxidation of Al presents its own issues. Fig. 3.3 shows a hugely increased (in terms of intensity and area) peak obtained after the 2nd sputter that is also shifted positively compared to the other sputtered results. The increase in area and shift have been identified as an Al/Al_2O_3 overlapping peak - where, compared to the dirty sample, there has only been a little oxide formation. The oxide is detected, as well as surface Al, thus blending the two peaks together to form one large, shifted peak.

This result compounds the necessity of providing proper UHV conditions, and has a direct effect on the compositional analysis.

Composition

Before the analysis of the compositional quantification is discussed, it is worth mentioning a couple of issues that give such measurements taken with XPS quite a large uncertainty value. The theoretical method of calculating these values has been discussed within section **2.3**, yet the precision was not detailed. When considering the many elements that such a seemingly simple calculation comprises of, it is easy to see why the uncertainty is usually given at around ±10%. Calculation of this uncertainty can be undertaken in a number of ways (using a Poisson distribution, using a 'residual' standard deviation, applying Monte Carlo simulations being just three [27]) which are built into CasaXPS. An example of how these methods work is contained within the appendix 5.6. For the basis of the analysis completed here, the uncertainty on the composition has been calculated using the standard deviation method contained within the appendix, which is the most accessible for a new user. Values calculated for each peak range from 1-10 %, so the largest values were used - all rounding up to ±10%. Consider: the 'spread' of the X-ray source energy, the resolution of the CHA, the precision of the RSF and IMFP values and, finally, the accuracy of the curve fitting used to calculated peak area. Each one of the components that are used when performing a compositional quantification have these respective uncertainties - it is no surprise that the results (obtained with XPS) have such a large uncertainty placed upon them. For example - if a QC was found to be composed of 5% Mn (a value not too unrealistic, as shown later), then, theoretically, and within the bounds of uncertainty, you could argue there is 0% Mn. Therefore, values calculated should be taken with a pinch of salt.

As previously discussed, the position of the Al2p region within the Al-Cu-Fe QC is a questionable source of analysis. Therefore, when it is patently clear that the values calculated for the composition are unreasonable, they will be compared to the acquisition of the Al2s region. As aforementioned, the composition of the surface of the Al-Cu-Fe quasicrystal is 63% Al, 24% Cu and 13% Fe respectively, and it is important to keep this original composition in mind when analysing the values calculated as large differences can give an indication as to how the surface reacts to sputtering/annealing.

The discrepancy between the Al2p and Al2s regions can be attributed to the overlapping of the Cu3p peak with the Al2p peak, interfering with the intensity that 'could' have been detected. That being said, the general trend for sputtering an alloy is that the lightest element gets preferentially sputtered (Al in this case), leaving a composition lower than the as-received composition. So, tab. 3.2 should display values lower than 63% for both core levels acquired. However, this only occurs for the Al2s level, compounding the difficulty the author had when calculating the area of the Al2p peak. Although, the values calculated are roughly consistent with each following sputter (bar the dirty scan) i.e. there is only a little deviance from the average - ∼70% for Al2p, ∼55% for Al2s. Happily, the 'true' value for the crystal as received is between these values and, with the 10% uncertainty, the discrepancy starts to look less bleak. Studies mentioned previously that investigated the oxidation of the QC's also looked at the composition of the Al-Cu-Fe and found similar results to those displayed in tab. 3.2 i.e. Al is preferentially sputtered away from the dirty sample - a result which is patently clear when collecting either the Al2p or Al2s regions [35]. The high percentage of Al as seen on the dirty sample is attributed to the segregation of the Al oxide layer from the bulk that effectively dominates the surface and effects peak acquisition. It could be said of the results displayed that, with the large uncertainty placed upon them, the actual values themselves aren't too important - only the trends that they display are.

3.1.2 Al-Cu-Fe Problems

A salient point that has been mentioned quite often over the course of this experiment (and indeed, in reference to UHV experiments in general) is that planning is essential, but plans are useless. In a nutshell, it doesn't matter the depth or intricacy of the plan, something can always throw a spanner in the works. Perhaps, because the nature of the work is highly reliant on a vast number of incredibly precise variables and intricate machinery, it is inevitable that issues arise. Thus, two sub-sections (one for each QC) have been dedicated to detailing the problems encountered during the experiments.

The first problem, although not a large one, affected the time-scale of the Al-Cu-Fe study and caused questions to be asked about the methanol delivery system - it is also an interesting physical problem. When testing the cold trap element of the methanol deposition, the vial that contains the methanol smashed when lowered into the liquid nitrogen bath. The vial had been lowered with the bottom of the vial parallel to the bath (i.e. straight down), causing the entire contents of the vial to freeze at the same time and, as liquid expands upon freezing, the methanol expanded at such a rate the vial was smashed. To counteract this phenomena, the vial was rotated by 45° to start a slow freeze at the corner of the vial, allowing a controlled freezing rate.

Secondly, an issue that had a direct effect on the results recorded was the quality of the vacuum reached - as previously mentioned, pressures in the main chamber only reached 3^{-9} mbar, not the ideal 10^{-10} mbar. This explains the presence of oxygen on the sample, despite being locked in the main chamber since introduction. The issue was simple; a pump was not working at full efficiency.

The final and most crucial problem: the limited results that are displayed for Al-Cu-Fe (small number of sputters relative to Al-Pd-Mn, no annealing) are due to the QC being destroyed via melting during the annealing process. The temperature of the sample and sample holder are measured using a temperature gun; by measuring the infra-red energy emitted from the object (and knowing its emissivity) the temperature of said object can be calculated. Using this gun, it was found that there was a difference in thermal conductivity between the holder and the sample that was greater than first thought. Thus, when the main chamber was brought up to annealing temperature (650K), the sample heated up beyond its melting temperature, despite the temperature gun reading a lower value. Upon melting and fusing with the holder, the Al-Cu-Fe sample was not fit for analysis and therefore this portion of the experiment had to be cancelled - switching the focus of the methanol deposition onto the Al-Pd-Mn quasicrystal.

3.2 Al-Pd-Mn Results

The results obtained from scanning the Al-Pd-Mn QC are presented within this section. Once again, using survey and core level spectra combined with compositional and peak position analysis, the following conclusions have been drawn. Oxygen and carbon contamination was once again found on the dirty sample, evidenced by the acquisition of the C1s and O1s core levels and the corresponding B.E. of Al_2O_3. Compositional analysis found values and a trend that agrees with previous literature [38], as well as presenting a segregation of Al_2O_3 at the surface, forming a passivity layer. This layer affected the acquisition of the Pd, Mn peaks on the dirty sample scan but, once removed through sputtering, allowed analysis on these peaks to be undertaken.

Once again, a survey spectra is presented to give an overall view of the sample.

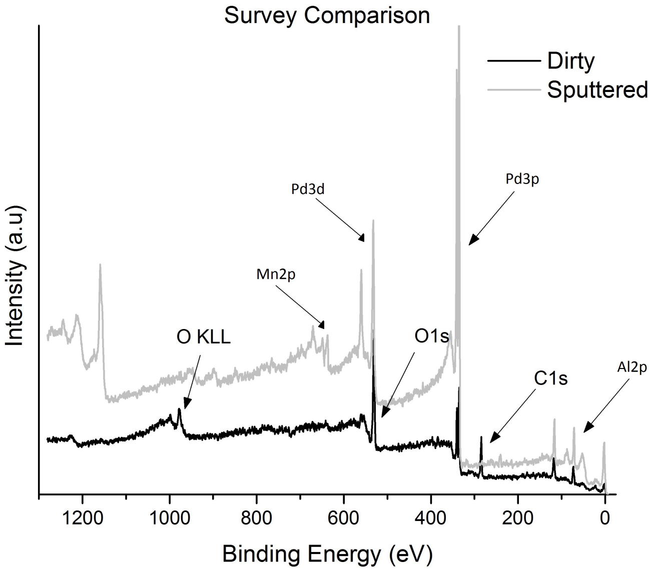

Figure 3.10: Survey comparison of the Al-Pd-Mn QC between dirty and sputter scans.

Compared to fig. 3.1, the peak shifts observed graphically are minimal at the most (unsurprising, given the peak position analysis). What is striking is the size (or lack thereof) of the Mn2p peak, which appears in the sputtered data. When enhanced on CasaXPS, there is a definite peak belonging to Mn2p - however on a survey scan (and, indeed, on fig. 3.18), this peak looks non-existent. Again, the intensities of the larger peaks is greatly increased, at the expense of the carbon and oxygen peaks; the Pd3p/O1s challenge is highlighted especially. The Al ‘region’ containing 2s, 2p and Auger peaks is more greatly pronounced - indeed, the Auger line is not visible on the dirty sample. Prominent, also, is the emergence of the Pd MNN Auger line - as highlighted in fig. 3.13b. Overall, fig. 3.10 provides a fantastic example of the effects of sputtering and how, without it, analysis of this sample would become nigh on impossible.

Presented here are the peak positions of each relevant peak found when survey scanning the Al-Pd-Mn quasicrystal, the uncertainties are again 0.1-0.2eV. The notation is as follows: Al2p is described as before, Pd3d is a concise description of Pd3$d_{5/2}$, likewise as Pd3p is technically Pd3$p_{3/2}$ and Mn2p is Mn2$p_{3/2}$; these notations are used for brevity.

	Binding Energy (eV)						Auger	K.E (eV)
	Al2p	Pd3d	$Pd3d_{3/2}$	Pd3p	$Pd3p_{1/2}$	Mn2p		Pd MNN
Elemental	72.8[26]	335.5[37]	340.3[38]	532.4[39]	560.2[39]	638.8[38]		327.4[40]
'Step'								
1	73.3	335.0	340.1	n/a	n/a	641.6		n/a
2	71.7	335.4	340.7	532.9	560.1	639.1		327.4
3	72.1	335.5	340.7	532.6	560.5	639.4		327.5
4	72.4	335.3	340.7	532.7	560.1	639.0		327.9
4	71.5	335.4	340.7	532.3	560.2	637.7		327.5
5	71.7	335.5	340.8	532.5	560.3	638.0		327.5
6	71.9	335.4	340.6	533.2	560.3	638.4		327.1
7	71.4	335.2	340.4	532.4	560.1	637.5		327.7
8	71.6	335.4	340.7	532.1	560.3	638.9		327.8

Table 3.3: Table consisting of data taken from the procedure outlined in tab. 2.2. Note: the first column is a key that corresponds to the step taken in tab. 2.2, hence, there are two '4' rows.

These peak positions show a drastic change between those collected from the dirty scan (step 1) and the subsequent sputtering. Peak shifts of up to a couple of eV are seen (particularly large is that of Mn2p - see fig. 3.12); large chemical shifts can be due to the formation of chemisorbed/physisorbed features at the surface, but can also be explained by signal-to-noise ratios - especially for Mn2p. From step 2/3 onwards the sample was considered clean, as the vacuum reached was of the required order and there is only a little evidence of oxygen/carbon from then on - particularly when the sample had been left for long periods of time (24 hrs and upwards), a phenomena expected when considering the time of contamination mathematics discussed within section **2.2**. The attributed oxide formed (Al_2O_3) at the surface is not featured in tab. 3.3 as its appearance is more erratic than that in tab. 3.1, likewise with the appearance of carbon. The discussion of finding evidence of oxygen in the scans is of importance yet again, but is a) a more complex analytical challenge (considering the overlap between O and Pd3p B.E.'s) yet b) hopefully has a clearer resolution than the oxidation issue discussed with the Al-Cu-Fe QC.

One particularly interesting aspect that can be gleaned from tab. 3.3 (in terms of intensity) is the 'emergence' of 2 specific peaks as the sputtering is performed: the Pd MNN line, and the Mn2p region. As will be shown, both are barely visible (or not at all visible when considering the background noise) on the dirty sample scan, yet become more intense as the sample is cleaned.

What follows is a series of graphs that cover a number of aspects that have been drawn from the data: the aforementioned emergence of the elemental peaks, the evolution of selected regions and an oxygen/carbon appearance study. Finally, the deposition of methanol onto the surface of the QC will be studied by detailed analysis of the C1s peak and the other various physisorbed species that are formed. The detection of C-O, C=O, C-C etc. will indicate if (and how) any methanol has decomposed at the surface - a feat that has not yet been attempted.

Fig. 3.11 shows the Al2p region evolution as the sample is sputtered, using data from selected surveys. The surveys have been arbitrarily picked, but provide a plot that is not

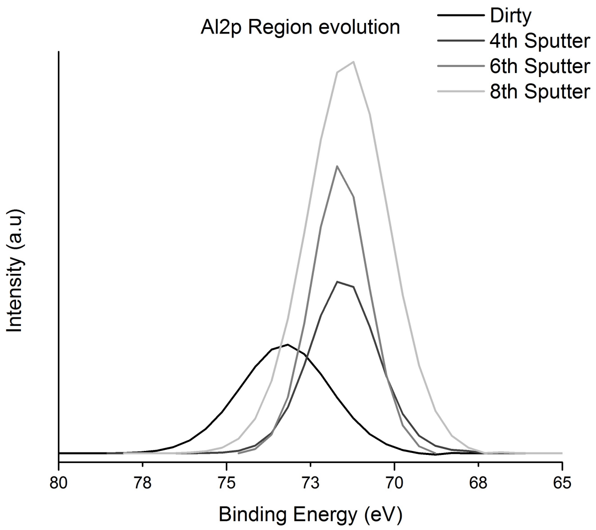

Figure 3.11: The evolution of the Al2p region, collected from the Al-Pd-Mn quasicrystal.

always dependent on the first 3 sputters (as seen in previous figures). Once again, the markedly large shift from the dirty scan compared to the sputtered sample scans are plain to see graphically, and suggests that Al_2O_3 has formed at the surface. The binding energy value for the peak obtained from the dirty sample given in tab. 3.3 corresponds with the oxide once again [32], and the absence of the Pd3p region on the dirty scan suggests that the oxide formation has completely dominated over other peaks (and perhaps other oxides). The peak shift for further scans are minimal, and oxygen rarely makes another position, suggesting that the shift for Al2p seen is due to a charge transfer that is inherent of the quasicrystalline structure of the sample - this point is discussed in the following sub-section. The increase in intensity is due to non-normalisation of the data, explained in the discussion.

The sputtered Mn2p peaks exhibit a drastic increase of both intensity and area of peak with respect to the dirty sample scan, quantitatively: $\sim$7 times more intense

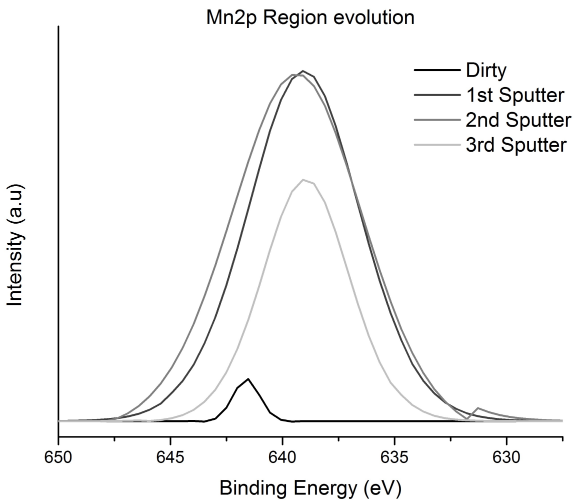

Figure 3.12: The Mn2p region evolution. Note the drastic intensity increase of the sputtered scan peaks from the dirty sample.

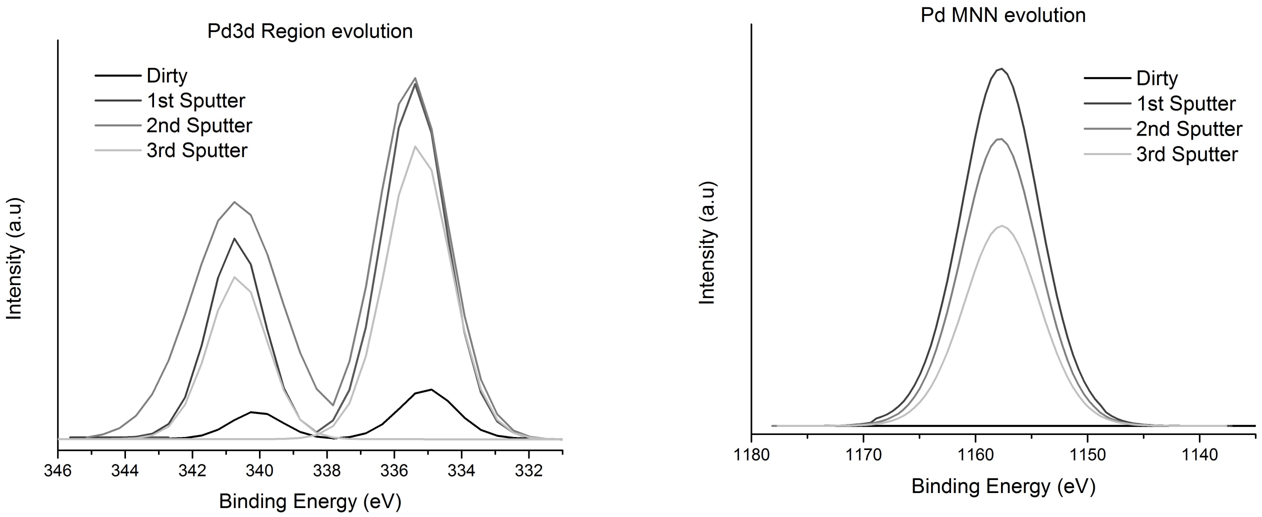

(a) Pd3d region evolution.

(b) Pd MNN auger electron evolution.

Figure 3.13: Collection of Pd graphs, detailing the most prominent region and auger electron evolutions.

∼30 times larger area. The dramatic rise is attributed to 2 issues surrounding the collection of the Mn2p region: the low signal-to-noise ratio of a dirty sample scan and the naturally low percentage composition of Mn in the QC (about 10 %). As always, these issues will be discussed in the following sub-section.

Again, the increase in intensity is large for the Pd3d region (fig.(3.13a)) following sputtering, although the evidence of any shifts is less obvious than figs. 3.11 and 3.12. Both peaks are fairly consistent in terms of peak position once the sample has been cleaned, shifting only a couple of 0.1 eVs (the uncertainty placed upon the results) throughout the scans. Noticeably, the two peaks shift synchronously i.e. if there is a shift then they will both negatively or positively shift together. Fig.(3.13b) shows the emergence of the Pd MNN auger line as the sample is sputtered: on the dirty scan there is no evidence, only background noise.

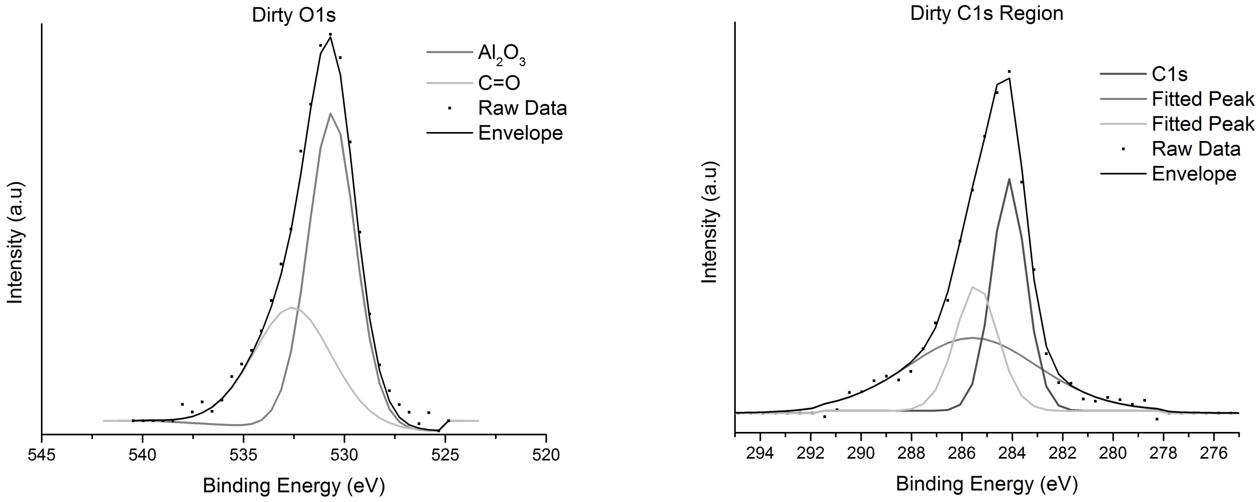

(a) Oxygen region from the dirty Al-Pd-Mn

(b) C1s region from the dirty Al-Pd-Mn

Figure 3.14: The oxygen/carbon peaks detected on the dirty Al-Pd-Mn sample. The presence of C=O can be determined on fig. 3.14a, but is less obvious on fig. 3.14b

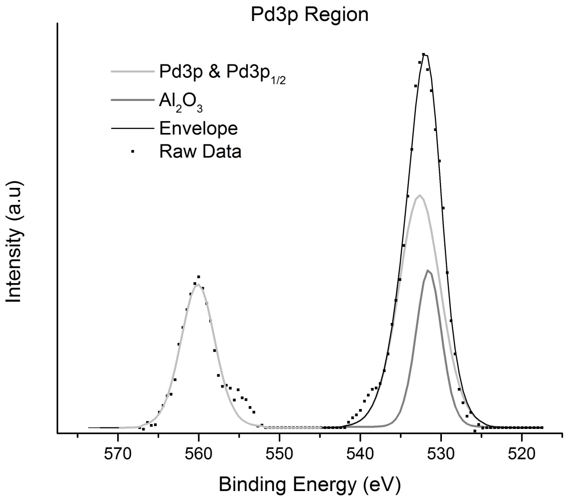

Figure 3.15: The Pd3p region that overlaps with the oxygen peak, as taken from the 3rd sputter.

Figs. 3.14a and 3.14b show the contamination at the surface of the Al-Pd-Mn QC, with the oxygen and carbon peaks shown respectively. C=O has been tentatively identified within the oxygen region in fig. 3.14a, as the peak created in CasaXPS lines up with the corresponding binding energy of ~533 eV [27]. Contradicting this identification is the lack of corresponding peak in the carbon region for C=O, as seen in fig. 3.7. Two fitted peaks have been added in an effort to match the raw data to the CasaXPS envelope, their peak positions do not correspond (directly) with known physisorbed species but have been tentatively identified as C-O-C and C-C bonds [27].

Fig. 3.15 shows the Pd3p region that overlaps with the binding energy of oxygen, as taken from the 3rd sputter. This graph illustrates the overlap of identified oxides (in this case Al_2O_3) with Pd3p - an analytical challenge that will be subject of discussion in the following section.

The composition of the crystal as it is sputtered is as follows:

	Composition %		
	Al	Pd	Mn
Step			
1	86	13	1
2	55	37	8
3	47	43	10
4	55	39	5
4	49	45	6
5	47	47	6
6	44	50	6
7	56	38	6
8	54	40	6
9	54	37	8

Table 3.4: Al-Pd-Mn composition percentage. Again, the doubling up of step 4 is due to the 2 scans that were taken in quick succession .

The composition of the 'as-grown' Al-Pd-Mn QC is: $Al_{70}Pd_{20}Mn_{10}$, and the hierarchy of the elements is clearly still being upheld, as shown in the above table. However, as seen in the sputtering of the Al-Cu-Fe, Al is preferentially sputtered away from the surface, increasing the composition of Pd. These results correlate with studies performed upon an oxidised Al-Pd-Mn QC which shows high Al concentration after oxidation (∼85%), as seen in the dirty scan composition (tab. 3.4, 1st step) [35]. Likewise when the sample is cleaned, Al is reduced at the gain of Pd, with Mn staying below 10%. The initial increase of Al at the surface from as-grown is attributed to the formation of Al oxides, as no other oxide is found on the scans, either by chemical shift or by analysis of the oxygen peak. Again, a graphical representation of tab. 3.4 is presented for clarity:

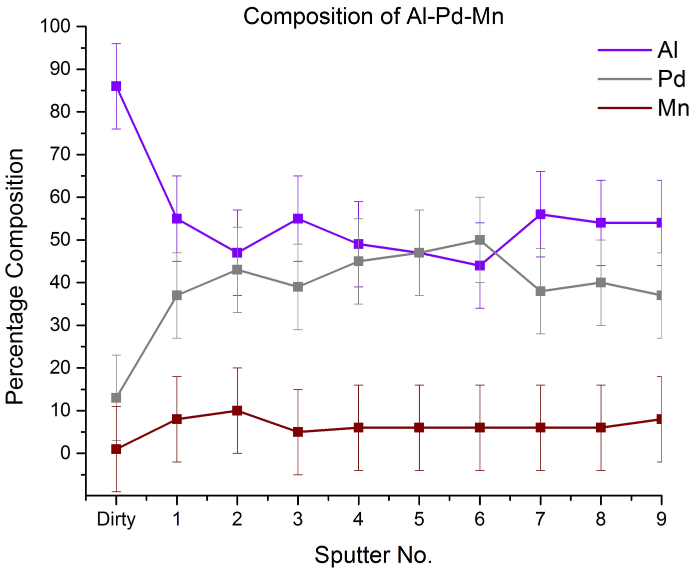

Figure 3.16: The composition percentages of the surface of the Al-Pd-Mn QC.

What is clear from fig. 3.16 is the lack of variance in the Mn composition when compared to both Al and Pd, which consistently have large changes in their percentages. This can be attributed to the respective peak acquisition - acquiring the Mn2p peak is a relatively simple process, as it is quite small and the effects of asymmetry are quite easy to account for. However, for higher intensity peaks such as Pd and Al, the effects of asymmetry become more pronounced and curve fitting becomes a more difficult challenge - increasing the likelihood of error.

3.2.1 Al-Pd-Mn Discussion

Al2p

As before with the Al-Cu-Fe QC, the Al2p region provides a basis for analysis beyond the scope of the planned experiment. An interesting peak position irregularity is observed, in that the 2p region is negatively shifted away from the elemental binding energy for Al2p, previously stated as 72.8 eV. Previous XPS studies performed upon icosahedral $Al_{70}Pd_{20}Mn_{10}$ find *positive* shifts of 0.2-0.27 eV for Al2p [41]-[42]. Now, as can be seen by the Al-Pd-Mn composition table, the sample scanned never reached the 'natural' ratio of 70:20:10 but - what is exciting regardless of the direction of the shift - is that there is a precedent for shifts in the icosahedral structure. To press this issue further, and to compare the measurements recorded by to previous experiments, the following study is presented: an as-grown $Al_{56}Pd_{36}Mn_8$ QC studied under XPS was found to present a shift for Al2p binding energy, pushing it up to 73.1 eV [38]. This compositional percentage is mirrored by the results obtained in step 2 - only differing by a 1% swing between Al and Pd - a step at which the recorded binding energy of Al2p was 71.7eV. The study reported little change in the Al2p B.E. from the pure metal value of 72.8 eV, however, a shift of 1.1eV is observed here. An argument could be made, therefore, that the shifts seen are due to the series of sputterings performed upon the QC, compared to the 'un-tampered' sample used in the study. Once annealed (thus easing out any defects and repairing the QC structure), the Al2p region is observed at 72.5 eV.

The increase in intensity as shown in fig. 3.11 is too marked and orderly to ignore and is not due to the reduction of sample contamination. What is theorised is that the data used to acquire the Al2p region for this sample was not normalised properly pre-analysis. Samples are usually scanned multiple times if they are of particular interest (i.e. scanned more regularly the cleaner they become) and, if not normalised, the intensity data builds up. The uniform way in which each peak appears to double in fig. 3.11 suggest that this has occurred.

The other peaks detected, as presented in tab. 3.3, exhibited no considerable shifts compared to their elemental B.E. values as the sample was cleaned.

Oxidation/Carbon Contamination

As before, the oxygen problem that arises with this QC will be discussed. The first point of issue is the aforementioned overlap between oxygen (binding energy lying between 529-535 eV depending on what is formed [27]) and Pd3p (binding energy of 532.4 eV). Clearly, on an oxygen contaminated palladium sample will exhibit both peaks - an oxide formation and the elemental Pd3p. Discerning the two and collecting the peak positions/areas correctly is important; knowledge of whether (and how) the surface has been affected by chemisorbed species gives an insight into any shifts that may occur.

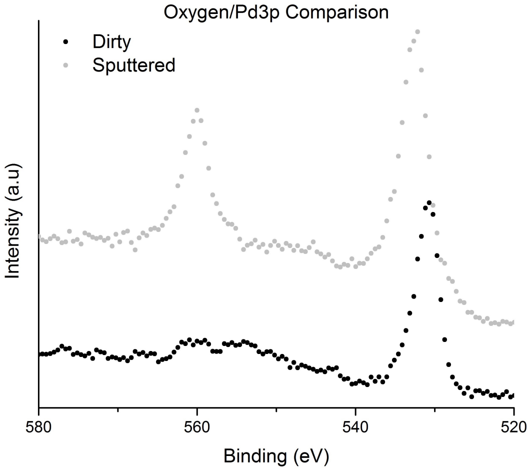

Figure 3.17: Comparison of the Pd3p region from dirty to sputtered.

The solution behind this discernment relates back to the multiplet splitting rules as outlined within tab. 2.1, in that the Pd3p peak will have double the area of the Pd3p$_{1/2}$ peak. From here on, the solution to obtaining the oxygen peak seems trivial; by acquiring the Pd3p$_{1/2}$ peak and then simply applying an area constraint that follows the 'doubling' rule on the Pd3p peak, any other peaks that need to be added will be clear to see. Fig. 3.15 demonstrates this technique, in that the Pd3p assigned peak does not make up the whole envelope of the data that is collected. Clearly, in this scan, oxygen is present, and a secondary peak needs to be included (identified by its B.E. as Al_2O_3) that creates an envelope that fits the raw data. Al_2O_3 is the only oxide identified across the survey scans using this technique, a result that is expected when studying previous literature [38]. On the dirty sample scan in fact, Pd3p is undetectable, (as seen in fig. 3.17) showing the oxygen peak only (i.e. Pd3p$_{1/2}$ is not seen). This does not indicate that Pd is not detected at the surface (made clear as the Pd3d region is collected), but rather highlights the effect that contamination can have when performing XPS experiments - had no other electron levels been detected for Pd, researchers could wrongly assume none was present.

In fig. 3.14a, C=O is attributed as the secondary peak to make up the envelope; its B.E. matches and as previously discussed, the peak could not be attributed to Pd3p with any certainty as Pd3p$_{1/2}$ is not seen to use as a reference. Casting doubts over this assumption is the analysis of the C1s region, as shown in fig. 3.14b. When performing curve fitting in CasaXPS, the two labelled fitted peaks were deemed necessary to fit the envelope to the raw data - otherwise the peak deemed to be C1s is shifted, and does not represent the shape the raw data forms. The issue with the two fitted peaks however is the non-correspondence of binding energy with any common physisorbed species, both falling around 285 eV. Of course, the asymmetric nature of most peaks presents a challenge for beginner users of CasaXPS wishing to avoid overuse of mathematical modelling.

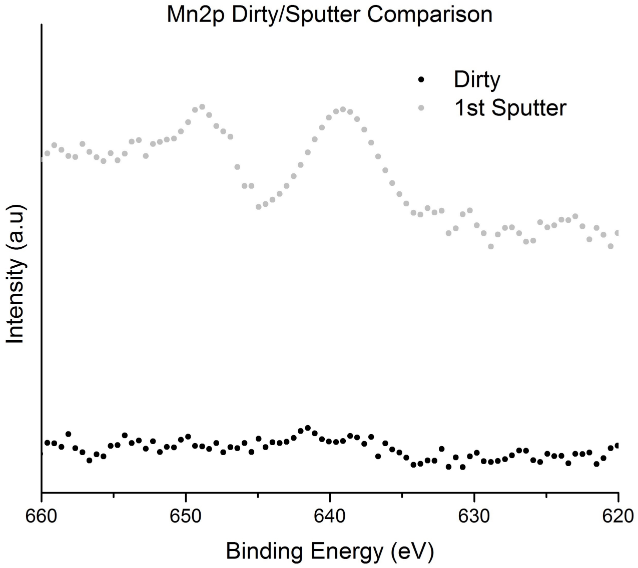

Figure 3.18: Comparison of dirty Mn2p to sputtered, to highlight the lack of peak.

Upon first glance, it could be suggested that Mn formed an oxide when studying the peak position between the dirty and sputtered sample, however, the large shift can be attributed to the low signal-to-noise ratio that was exhibited on the dirty scan. Figs. 3.12 and 3.18 show this effect and highlight the difficulty of analysing a sample with a particularly low concentration, sensitive element.

Finally, the segregated layer of Al_2O_3 that forms at the surface (as previously discussed within the Al-Cu-Fe discussion section) has been identified as the reason behind the intensity increase seen in the Pd and Mn core level peaks. This layer dominates over the surface, meaning it is difficult to excite the Pd and Mn electrons - leading to decreased intensity. The effect of the passivating layer being sputtered away is clear to see from all the figures contained within the results section.

Composition

In comparison to the compositions calculated for Al-Cu-Fe, the Al-Pd-Mn values follow a similar trend - in that the Al-dominated dirty surface (due to oxide formation) is steadily reduced to a plateau percentage (~51%), allowing the more catalytically reactive element (Pd in this case) to exhibit itself. Likewise, the passivity layer of segregated Al_2O_3 shows itself again with the high percentage (86%) of Al on the dirty sample. The behaviour of both QC's in this manner is promising, and perhaps explains why the surface reacts so well to the leaching process for Al-Cu-Fe. As previously mentioned, an important part of the leaching of the sample is the de-oxidation of Al; re-oxidation is vital to the steam reforming of methanol. As the de-oxidation (performed here by sputtering) of the sample reduces the percentage of Al in the composition and increases the percentage of Pd, it could be said the sputtering the QC is indeed as critical as leaching for preparation as use as a catalyst. Indeed, the plan for depositing methanol is based around creating a rough sputtered surface for the methanol molecules to stick to; by 'creating' more Pd atoms per unit surface area, the activity of the QC can only increase. Studies of cubic Al-Pd-Mn have shown that all 3 elements in the surface more readily oxidise than compared to icosahedral Al-Pd-Mn - suggesting the structure at the surface prevents Pd and Mn from oxidising, hence increasing its catalytic activity [38]. Leaching is, of course, still hugely important in this process, as it 'protects' the surface from becoming hugely dominated by Al_2O_3 once decomposition of methanol takes place.

Mentioned several times previously, the acquisition of the Mn2p peak was made quite challenging due to the low signal-to-noise ratio inherent on survey scans when involving particularly weak intensity peaks. The low percentage composition of Mn expected when analysing an icosahedral form of Al-Pd-Mn was found - although the 1% value for the dirty scan must be taken with a pinch of salt, when considering the peak used to obtain such a result (see fig. 3.18). As the sputtering continued however, the value calculated was pleasingly close to as-grown percentages - certainly within the realm of the uncertainties placed upon compositional calculations.

Overall, the percentages post-dirty sample show only a small variance between sputters, i.e., towards the final sputters a natural compositional ratio of 50:40:10 was reached. When compared to previous studies, this ratio is a little dissimilar; 70:20:10 appears to be the accepted value from an anneald Al-Pd-Mn QC (of course, this is the same as the as-grown

QC) [38]. It is believed that loss of quasicrystalline structure at the surface is the causation behind this difference, caused in turn by the heavy amount of sputtering the surface had to endure. Indeed, annealing the QC returns the quasicrystalline structure to the surface and gives a composition of $\sim$ 70:20:10, demonstrated by tab. 3.5. The peak positions are also presented, with a view to showing how annealing may change them.

	Al2p	Pd3d	Mn2p
Composition (%)	72	21	7
Peak Postion (eV)	72.8	336.8	638.6

Table 3.5: Compositional calculations and peak positions for the annealed Al-Pd-Mn.

Pleasingly, the composition reverts to values very close to the as-grown QC. The Al2p peak demonstrates a B.E. that agrees with literature studying the region, whilst Mn2p displays a shift of only 0.2 eV - the upper estimate of the uncertainty [26]. The Pd3d region exhibits a considerable positive shift however, of 1.3 eV - a shift and peak position not seen on previous sputtered scans (see tab. 3.3). Considering how clean the sample appears pre-anneal (no contaminations and highly accurate peak positions when compared with scientific literature) and, presuming the sample is clean post-anneal (again no contaminants, and no reason *why* it should be contaminated) - this shift must be due charge transfer at the surface due to the quasicrystalline structure reforming. Previous studies of a similarly composed Al-Pd-Mn QC (70:21:9) found positive shifts of up to 1.8 eV [35] for the Pd3d peak - reinforcing the value obtained from the annealed sample, and the theory that the structure at the surface is causing this transfer. It can be theorised further that the oxidation of the sample affected the early values obtained in tab. 3.3, and the consequent heavy sputtering ruined the icosahedral structure at the surface - giving binding energies expected of cubic structures. The anneal data displaying the shift is presented in fig. 3.19, with fig. 3.20 giving a survey spectrum comparison.

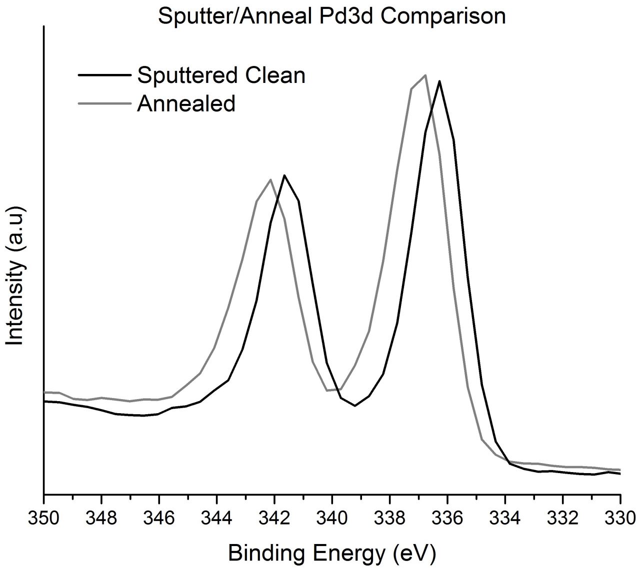

Figure 3.19: Pd3d peak between last sputter and 1st anneal, showcasing the peak shift.

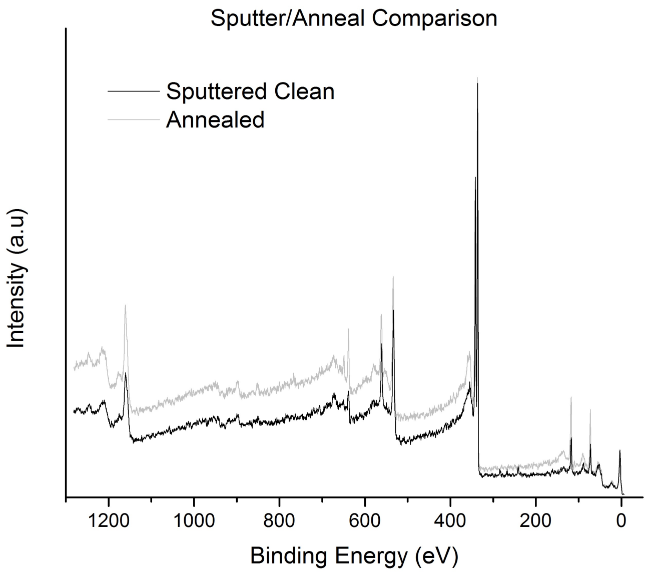

Figure 3.20: A survey spectrum comparison between the last sputter and 1st anneal.

What is immediately clear is that, even when completely clean, annealing the sample increases the intensity of peaks recorded still further. Apart from this intensity increase however, the surveys are unerringly similar (aside from the Pd3d shift, not resolvable in fig. 3.19). This example of annealed data rubber stamps the need for the sputter/anneal cycle when conducting XPS analysis - as each scan (from dirty) has increasingly given higher intensity peaks with a low signal-to-noise ratio.

3.2.2 Al-Pd-Mn Problems

What is patently clear, from the absence of results and discussion on the matter, is that the deposition of methanol could not be completed in time for the writing of this thesis. Thus, with a view to explaining why the focal point of the study was not undertaken, the various problems that were encountered during the course of the experiment will be detailed. Although none were as costly (in terms of resources) as the Al-Cu-Fe melt, several issues caused the progress of the Al-Pd-Mn study to be delayed and, at times, halted.

Primarily, and most damagingly, 2 critical components within the UHV instrumentation broke during the course of the Al-Pd-Mn study. First, the X-ray filament contained within the X-ray source broke, making XPS measurements completely impossible. The filament is used to produce the initial electrons that bombard and excite the anode material, which (usually) would then emit the desired X-rays. Following this damage, the experiment was placed on hold for a further two weeks. Secondly, and less detrimental to progress: the pre-amplifier used to enable stable low current operation (more commonly used in STM experiments) broke. Although a small issue, this still held up the experiment by a further week. The major problem that is presented with both breakages (aside from cost and labour associated with replacing them) is having to bring the entire system back to atmospheric pressure in order to fix/replace the components; controlled pressurisation takes time. Following from this, the entire system has to be baked and degassed in order to remove any contaminants that may have been picked up during maintenance. Baking the system takes 5-6 days; it takes 2-3 days to heat, then 2-3 days to cool. As evidenced, the complexity of these experiments is to such a level that even the smallest mistakes/breakages can cause long outlays.

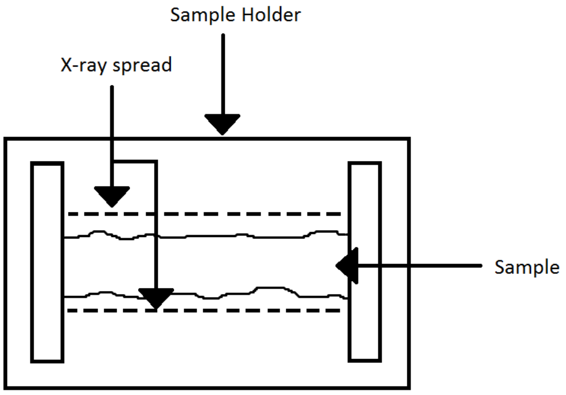

Figure 3.21: Schematic illustrating the sample plate scan problem.

Highlighted in tab. 2.2 for further discussion were the 'test scan' and 'sample plate' scan. To put these procedures in context, it is worth explaining a problem that was found when first scanning the Al-Pd-Mn sample. Initial survey scans (not included in this report as they were discarded) displayed a lot of noise and unexplained peaks, i.e. peaks that couldn't be explained by physi or chemisorbed species. Upon further inspection, it was found that the orientation of the QC on the sample holder was such that the X-rays used to scan had a broader width than the width of the sample (see fig. 3.21). This phenomena meant that the scans were 'contaminated' with the elements that made up the sample holder. Correcting this error took careful consideration of the positioning of both holder and sample, as well as the fine-tuning of the targeting of the X-rays used.

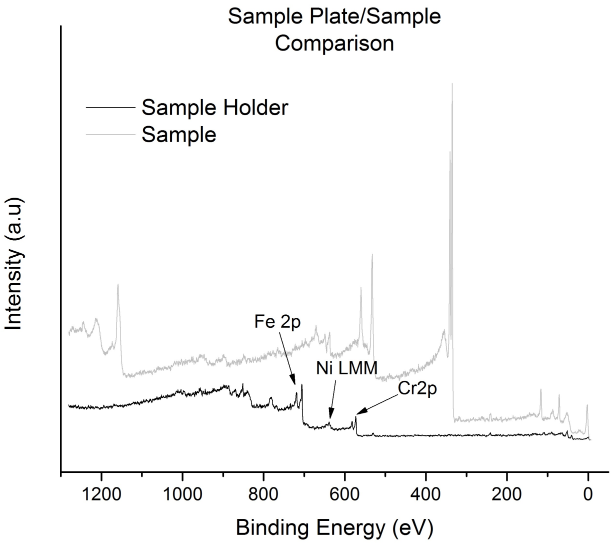

Figure 3.22: Survey scan showing the differences between sample and sample holder. Note the peaks that could have caused confusion, as labelled.

Using CasaXPS, the sample holder was tentatively found to consist of Fe, Ni and Cr. Of course, the exact elemental make-up is of no importance, and this figure simply serves as an interesting side-point. It can be clearly seen, however, how this problem could have affected the outcome of the study as a whole.

Finally, a series of power-cuts that the laboratory and University had to endure during the experiment effectively destroyed (or made unattainable) a large quantity of data (including several survey scans of the annealed Al-Cu-Fe pre-melt). The power-cuts were responsible for the hard drive used to store the data failing and, of course, beyond the nuisance of the lost data, the power loss meant that the pumps operating cut out. Hence, the vacuum in the chambers was lost, causing contamination; the whole baking, pumping and preparation process had to start again. It would be reasonable to assume that these power-cuts were also responsible for the filament and pre-amplifier issues, additionally.

Chapter 4

Conclusion

An analytical study of two quasicrystals using XPS has been presented, with the initial (unfortunately incomplete) aim to investigate how they reacted to the deposition of methanol at their surfaces. This primary goal is still a hot topic within the catalysis/quasicrystal industry, so it is unfortunate that evidence cannot be presented here which supports the use of using QCs in the production of hydrogen. However, analysis on the C1s peak detected on the dirty samples has leant valuable experience to the author and will only serve as an advantage for further studies on this matter. As a way of compensating for the lack of methanol results, the effects of sputtering and annealing on these surfaces has been demonstrated - with particular detail being taken over surface composition and binding energy values of the surface elements. As such, the following deductions are made.

The sputtering of both QCs (using both sets of results for Al-Cu-Fe) led to an overall decrease in Al surface composition. Comparisons with referenced literature and further survey scans that exhibit no or less oxygen have led to the conclusion that, as Al_2O_3 is sputtered away, the Al composition is reduced with it. This is due to the segregation of said Al oxide layer from the surface producing a large composition percentage on the dirty sample scan. The reduction from this high percentage value corresponds to results seen in previous studies - although the results obtained for the Al2p core level were deemed unreliable. The reduction of Al at the surface allows the classically more active components of the QCs (Cu [noted for its involvement in previous methanol studies] and Pd respectively) to have a larger presence at the surface. Thus, it is noted that sputtering the samples is a key process before the theoretical deposition of methanol.

Binding energy shifts were evidenced on both QCs. For the Al-Cu-Fe, the shifts seen in the Al2p region have been found to be dependent on the interference of the nearby Cu3p peak, or the formation of Al_2O_3 - the former being more likely, as little evidence is found of oxygen contamination on the larger B.E. shift scans. While this particular shift provided a challenge, the conclusions made are murky and neither outcomes are particularly interesting or engaging. However, the shifts seen in the Al-Pd-Mn scans are of much more interest. The Al2p region is affected once more, with negative shifts seen during the sputtering used to clean the surface. It is believed that by the end of the initial scans the sputtering had taken its toll on the crystal and destroyed the quasicrystalline structure at the surface. The shifts seen could be due to the mêleé of structures caused by this damage - for instance, if QC structure is damaged and a new 'quasi'-quasistructure is formed, the bonds between the elements have been changed, leading to B.E. shifts, as evidenced. Once annealed (and thus restoring QC structure), the Al2p peak is observed at the classically known value, lending this theory some weight. However, upon annealing, Pd3d has shifted. This result is expected when compared to previous studies on similarly composed Al-Pd-Mn, and is due charge transfer at the surface due to the quasicrystalline structure. It is likely that this shift is only observed on the annealed sample because of the previous damage of the surface structure incurred during sputtering.

Overall, the work performed provided the author with a large amount of experience in the field of UHV and surface science studies. However, it is unfortunate and a shame that the deposition of methanol could not be performed due to the aforementioned problems. Nevertheless, the continuing of this work in a PhD role will (hopefully) allow the initial experiment to be completed and will no doubt provide additional training. It is believed that the deposition on Al-Pd-Mn will be used as a 'mini-project' at the start of the PhD, with a possibility of the outcome to be published.

Bibliography

[1] D. Shechtman et al. *Metallic Phase with Long-Range Orientational Order and No Translational Symmetry.* Physical Review Letters, 53(20), 1984.

[2] Bindi et al. *Natural quasicrystal with decagonal symmetry.* Nature, Scientific Reports, 5(9111), 2015.

[3] U. Grimm, M. Baake. *Mathematical diffraction of aperiodic structures.* Chem Soc Rev, 41(20), 2012.

[4] A.P. Tsai. *Highly active quasicrystalline Al-Cu-Fe catalyst for steam reforming of methanol.* Applied Catalysis A: General, 214(2), 2001.

[5] Z. Barlow. *Breakthrough in hydrogen fuel production could revolutionize alternative energy market.* www.vtnews.vt.edu/articles/2013/04/040413-cals-hydrogen.html, 2013. Date Accessed: 22/03/2015

[6] M. Raney. *US 1628190*, 1926.

[7] M. Armbrüster et al. *Intermetallic compounds in heterogeneous catalysis: a quickly developing field.* Science and Technology of Advanced Materials, 15(3), 2014.

[8] A.P. Tsai, S. Kameoka, T. Tanabe. *Al-Cu-Fe quasicrystals for steam reforming of methanol: a new form of copper catalysts.* Catalysis Today, 93-95(1), 2004

[9] A.P. Tsai, T. Tanabe, S. Kameoka. *Microstructure of leached Al-Cu-Fe quasicrystal with high catalytic performance for steam reforming of methanol.* Applied Catalysis A: General, 384(1-2), 2010.

[10] M.Lowe et al. *Influence of leaching on surface composition, microstructure, and valence band of single grain icosahedral Al-Cu-Fe quasicrystal* . The Journal of Chemical Physics, 142, 2015.

[11] G.P. Parravicini, G. Grosso. *Solid State Physics.* Academic Press, 2013.

[12] B. Hankamer, M.J. Landsberg. *Symmetry: A guide to its application in 2D electron crystallography.* Journal of Structural Biology, 160(3), 2007.

[13] H.C. Jeong P.J Steinhardt. *A similar approach to Penrose tiling with implications for quasicrystal formation.* Nature, 382(6590), 1996.

[14] P.J. Steinhardt D. Levine. *Quasicrystals I. Definition and Structure.* Physical Review B, 34(2), 1986.

[15] P. van der Heide. *X-Ray Photoelectron Spectroscopy : An Introduction to Principles and Practices.* John Wiley and Sons, 2011.

[16] C.R. Nave. *Hyperphysics.* http://hyperphysics.phy-astr.gsu.edu/hbase/hph.html, 2001. Date Accessed: 09/05/2015

[17] N. Fairley. *CasaXPS Manual 2.3.15.* Casa Software Ltd, 2009.

[18] W.A. Dench M.P. Seah. *Quantitative electron spectroscopy of surfaces: a standard data base for electron inelastic mean free paths in solids.* Surface and Interface Analysis, 1(1), 1979.

[19] J. O'Connor et al. *Surface Analysis Methods in Materials Science.* Springer Science and Business Media, 2003.

[20] W.J. Moore. *Physical Chemistry.* Longman, 1972.

[21] S. Tanuma et al. *Calculations of electron inelastic mean free paths.* Surface and Interface Analysis, 21(3), 1994.

[22] J.F. O'Hanlon. *A User's Guide to Vacuum Technology.* J. Wiley and Sons, 2003.

[23] C. A. M. Brenninkmeijer. *Automated variable temperature liquid nitrogen cold trap.* Analytical Chemistry, 54(14), 1982.

[24] M.G. Cook, N.S. McIntyre. *X-ray photoelectron studies on some oxides and hydroxides of cobalt, nickel, and copper.* Analytical Chemistry, 47(13), 1975.

[25] J.L. Sullivan, P. Mills. *A study of the core level electrons in iron and its three oxides by means of X-ray photoelectron spectroscopy.* Journal of Physics D: Applied Physics, 16(5), 1983.

[26] R. Haeurt et al. *XPS investigation of the a-C : H/Al interface.* Surface Science, 292(1-2), 1993.

[27] Thermo Scientific XPS Database. Date accessed: *06/04/2015.*

[28] C.D. Wagner. *Chemical shifts of Auger lines, and the Auger parameter.* Faraday Discussions of the Chemical Society, 60(291), 1975.

[29] Biesinger et al. *Resolving surface chemical states in XPS analysis of first row transition metals, oxides and hydroxides: Sc, Ti, V, Cu and Zn.* Applied Surface Science, 257(887), 2010.

[30] Z. Bastl and S. Černý. *X-ray photoelectron spectroscopy study of the interaction of carbon monoxide and propylene with dysprosium and yttrium surfaces* Journal of Alloys and Compounds, 1(176), 1991.

[31] M. P. Seah, M. T. Anthony. *XPS: Energy calibration of electron spectrometers. 2Results of an interlaboratory comparison.* Surface and Interface Analysis, 6(3), 1984.

[32] Y. Huttel et al. *Intermediate oxidation state with substoichiometric Al oxide and a non-abrupt Al2O3/Al interface.* Applied Physics Letters, 62(2437), 1993.

[33] B. Ealet, E. Gillet. *Characterization of sapphire surfaces by electron energy-loss spectroscopy.* Surface Science, 273(3), 1992.

[34] P.E. Larson. *X-ray induced photoelectron and auger spectra of Cu, CuO, Cu2O, and Cu2S thin films.* Journal of Electron Spectroscopy and Related Phenomena, 4(3), 1974.

[35] C.J. Jenks et al. *Proceedings of the Conference on New Horizons in Quasicrystals: Research and Application.* World Scientific, 1997.

[36] M.W. McDowell R.A. Rosenberg. *2219 Aluminium Alloy by XPS.* Surface Science Spectra, 2(113), 1993.

[37] A.M. Venezia et al. *Particle size and metal-support interaction effects in pumice supported palladium catalysts.* Applied Catalysis A: General, 125(1), 1995.

[38] C.J. Jenks et al. *Photoelectron spectra of an Al-Pd-Mn quasicrystal and the cubic alloy Al-Pd-Mn.* Physical Review B: Condensed Matter and Material Physics, 54(9), 1996.

[39] S.J. Simko, M.C. Militello. *Elemental Palladium by XPS.* Surface Science, 387(3), 1994.

[40] J.M. Trooster, P.M. van Attekum. *Bulk- and surface-plasmon-loss intensities in photoelectron, Auger, and electron-energy-loss spectra of Mg metal.* Physical Review B: Condensed Matter and Material Physics, 20(6), 1979.

[41] Zurkirch et al. *XPS and EELS study of a quasicrystalline Al70Pd20Mn10 alloy.* Journal of Electron Spectroscopy and Related Phenomena, 7(3), 1996.

[42] Zhang et al. *Electronic structure of icosahedral Al 70 Pd 20 Mn 10.* Physical Review B: Condensed Matter and Materials Physics, 50(10), 1994.

Chapter 5

Appendix

5.1 Restriction Theorem

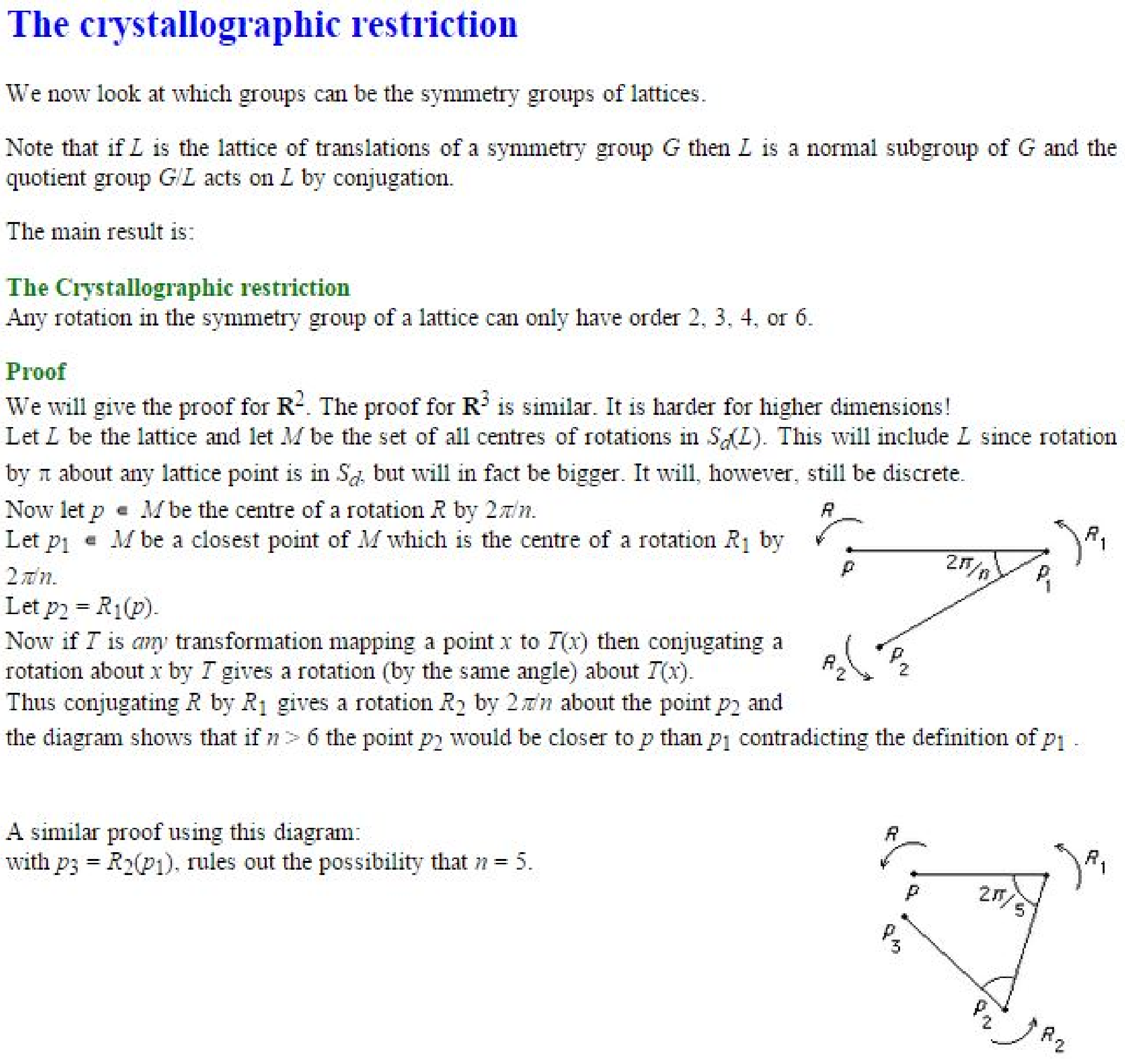

The crystallographic restriction

We now look at which groups can be the symmetry groups of lattices.

Note that if L is the lattice of translations of a symmetry group G then L is a normal subgroup of G and the quotient group G/L acts on L by conjugation.

The main result is:

The Crystallographic restriction
Any rotation in the symmetry group of a lattice can only have order 2, 3, 4, or 6.

Proof
We will give the proof for $\mathbf{R}^2$. The proof for $\mathbf{R}^3$ is similar. It is harder for higher dimensions!
Let L be the lattice and let M be the set of all centres of rotations in $S_d(L)$. This will include L since rotation by π about any lattice point is in S_d, but will in fact be bigger. It will, however, still be discrete.
Now let $p \in M$ be the centre of a rotation R by $2\pi/n$.
Let $p_1 \in M$ be a closest point of M which is the centre of a rotation R_1 by $2\pi/n$.
Let $p_2 = R_1(p)$.
Now if T is *any* transformation mapping a point x to $T(x)$ then conjugating a rotation about x by T gives a rotation (by the same angle) about $T(x)$.
Thus conjugating R by R_1 gives a rotation R_2 by $2\pi/n$ about the point p_2 and the diagram shows that if $n > 6$ the point p_2 would be closer to p than p_1 contradicting the definition of p_1.

A similar proof using this diagram:
with $p_3 = R_2(p_1)$, rules out the possibility that $n = 5$.

Taken from John O' Connor's series of lectures on crystallographic structure. (School of Mathematics and Statistics, University of St. Andrews Scotland, 2003)

5.2 Icosahedron

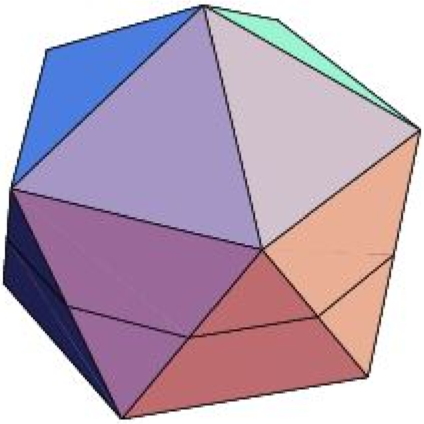

Icosahedral structure in 3 dimensions.

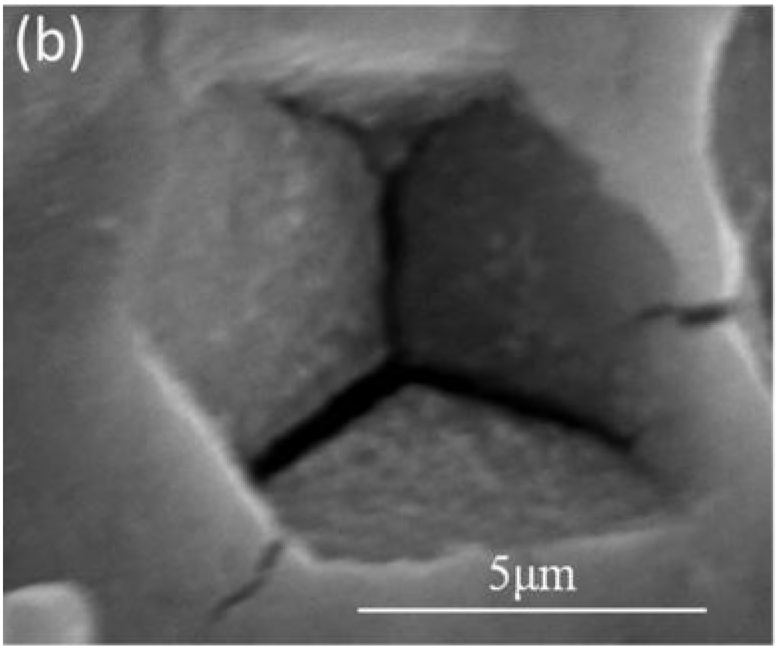

Icosahedral structure witnessed at the surface of a leached Al-Cu-Fe QC. Obtained via TEM [10].

5.3 Pump schematics

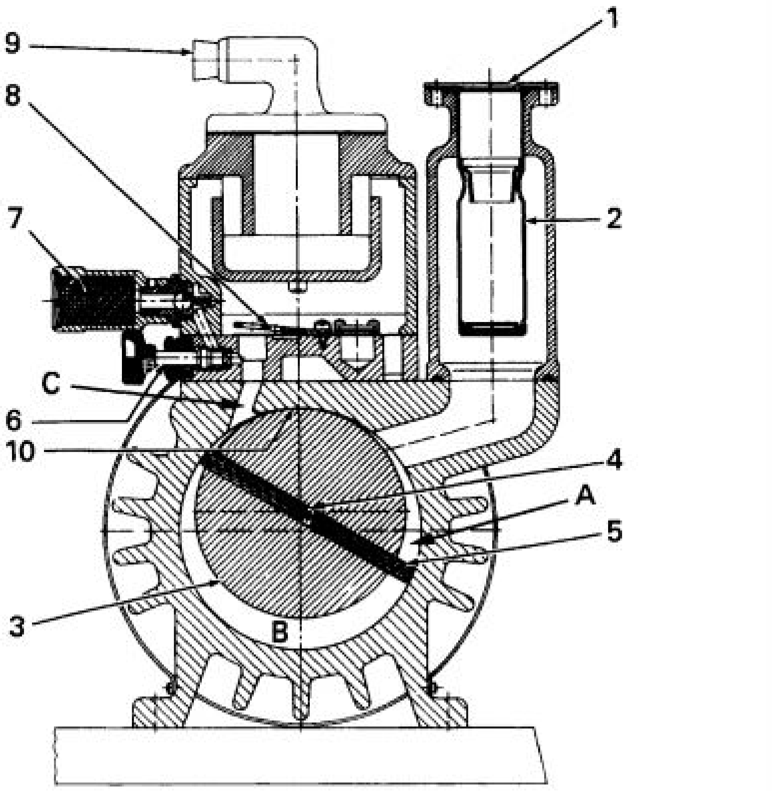

Fig. 10.1 Sectional view of the Pfeiffer DUO-35, 35 m3/h double-stage, rotary vane pump: (1) intake, (2) filter, (3) rotor, (4) spring, (5) vane, (6) gas ballast valve, (7) filter, (8) discharge valve, (9) exhaust, (10) sealing surface. Reprinted with permission from A. Pfeiffer Vakuumtechnik, GmbH, Wetzlar, Germany.

Rotary Pump [22].

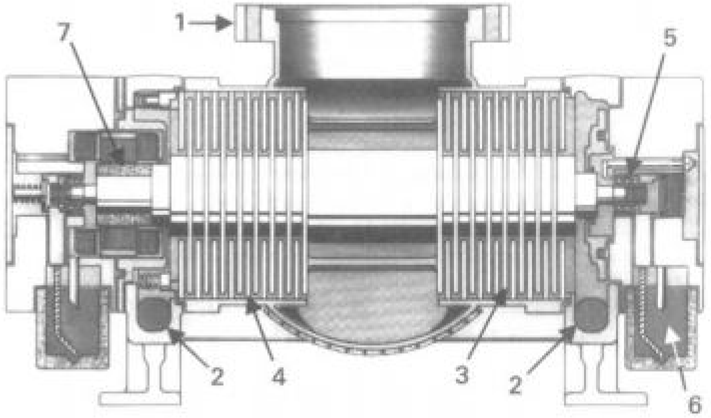

Fig. 11.1 Section view of Pfeiffer TPU-200 turbomolecular pump: (1) inlet, (2) outlet, (3) rotor disk, (4) stator disk, (5) bearing, (6) oil reservoir, (7) motor. Reprinted with permission from A. Pfeiffer Vakuumtechnik, GmbH, Wetzlar, Germany.

Turbomolecular Pump [22].

5.4 Log of Procedures

Presented below is the log of procedures for the Al-Cu-Fe QC as performed by Dr. Paul Unsworth.

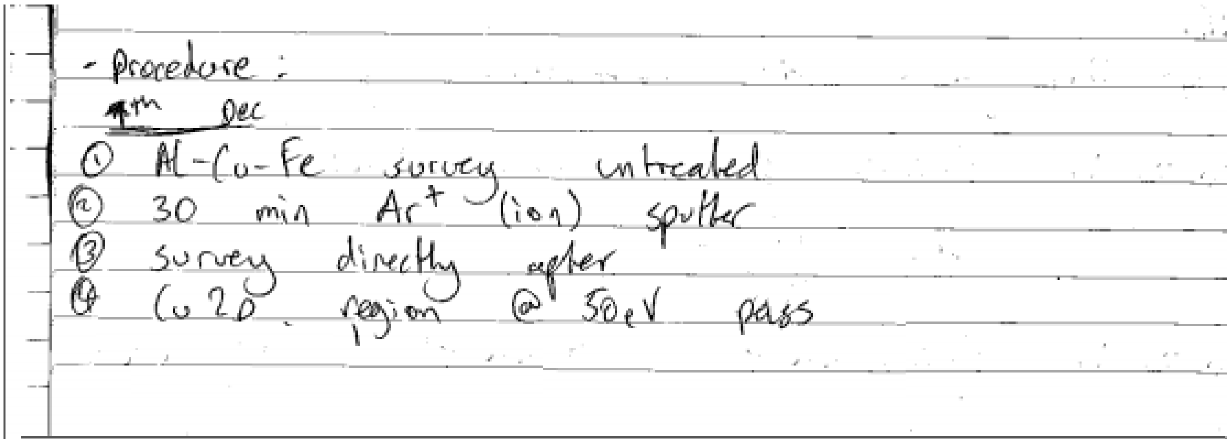

- Procedure :

7th Dec

① Al-Cu-Fe survey untreated

② 30 min Ar^+ (ion) sputter

③ survey directly after

④ Cu 2p region @ 50eV pass

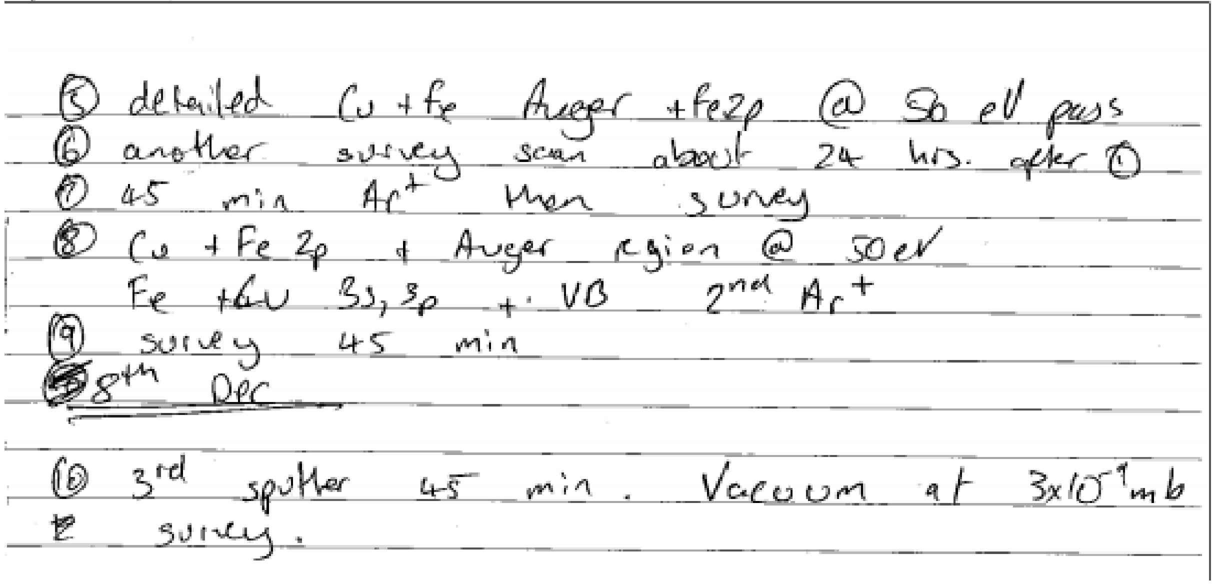

⑤ detailed Cu + Fe Auger + Fe2p @ 50 eV pass

⑥ another survey scan about 24 hrs. after ①

⑦ 45 min Ar^+ then survey

⑧ Cu + Fe 2p + Auger region @ 50eV

Fe + Cu 3s, 3p + VB 2nd Ar^+

⑨ survey 45 min

8th Dec

⑩ 3rd sputter 45 min. Vacuum at 3×10^{-9} mb

& survey.

5th Jan Monday.

Start 45 min 5th Ar Sputter. Vac. 2.10^{-10} mb
$_{\text{Mc}}$

Sample Now Clean.

⑭ AlCuFe Survey after 5th Ar Sputter.

~~⑮ AlCuFe Cu3p and Al2p after 5th Sputter (45min) 20eV Pass.~~
Crashed computer trying to save file.

✓ ⑮ AlCuFe Cu3p, Al2p, and Fe3p 20eV Pass.

12th Jan Monday

Continue degassing sample e heater stage.
650°C by pyrometer (emissivity 0·35)
2·1 amps thro' heater. 7.10^{-9} mb − P_{prep}

✓

⑯ [illegible] AlCuFe Survey after heating to 680°C for 30 mins
$P_{prep} = 9.10^{-9}$ mb.

I think Aluminium has segregated to surface.!!

✓

⑰ ~~⑯~~ AlCuFe Cu3p, Al2p and Fe3p after Al seg.

~~⑰~~.

~~⑱ AlCuFe Survey Scan after Al seg.~~

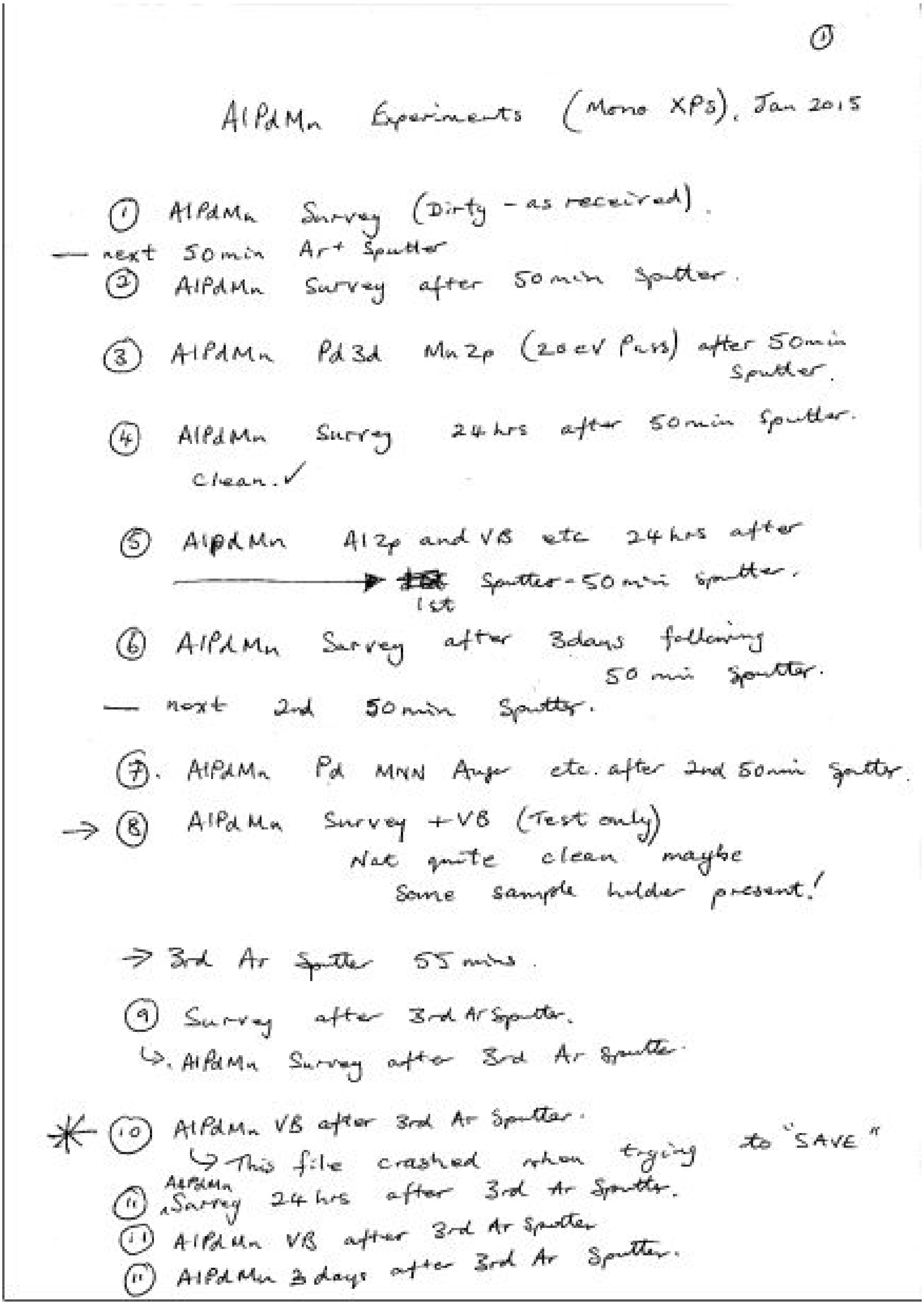

①

AlPdMn Experiments (Mono XPS). Jan 2015

① AlPdMn Survey (Dirty - as received).

— next 50min Ar+ Sputter

② AlPdMn Survey after 50min Sputter.

③ AlPdMn Pd 3d Mn 2p (20eV Pass) after 50min Sputter.

④ AlPdMn Survey 24hrs after 50min Sputter.
clean. ✓

⑤ AlPdMn Al 2p and VB etc 24hrs after
→ 1st Sputter - 50min Sputter.

⑥ AlPdMn Survey after 3days following 50 min Sputter.

— next 2nd 50min Sputter.

⑦. AlPdMn Pd MNN Auger etc. after 2nd 50min Sputter.

→ ⑧ AlPdMn Survey + VB (Test only)
Not quite clean maybe
Some sample holder present!

→ 3rd Ar Sputter 55 mins.

⑨ Survey after 3rd Ar Sputter.
↳. AlPdMn Survey after 3rd Ar Sputter.

✳ ⑩ AlPdMn VB after 3rd Ar Sputter.
↳ This file crashed when trying to "SAVE"

⑪ AlPdMn Survey 24 hrs after 3rd Ar Sputter.

⑪ AlPdMn VB after 3rd Ar Sputter

⑪ AlPdMn 3 days after 3rd Ar Sputter.

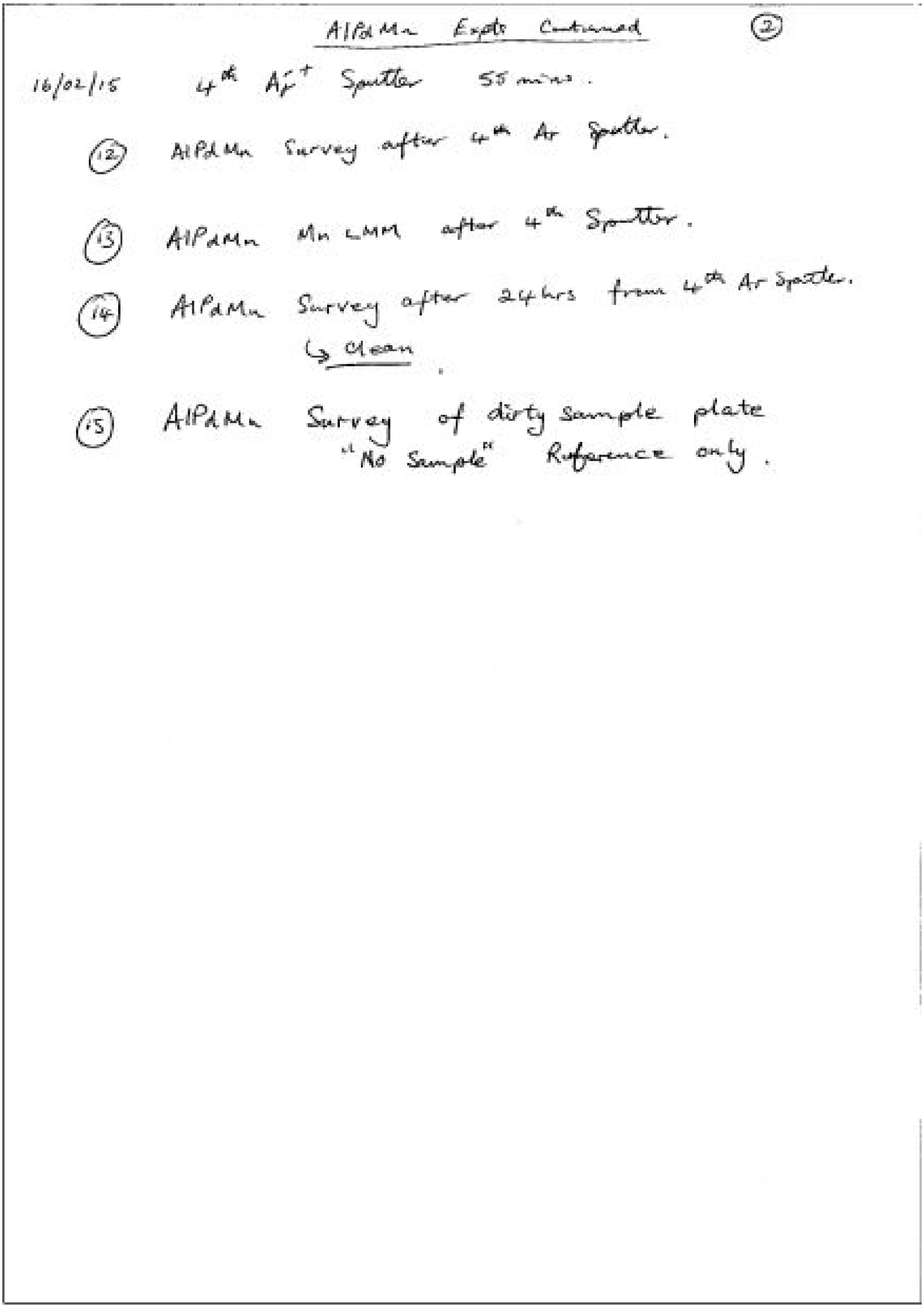

AlPdMn Expts Continued ②

16/02/15 4th Ar$^+$ Sputter 55 mins.

⑫ AlPdMn Survey after 4th Ar Sputter.

⑬ AlPdMn Mn LMM after 4th Sputter.

⑭ AlPdMn Survey after 24hrs from 4th Ar Sputter.
↳ Clean.

⑮ AlPdMn Survey of dirty sample plate
"No Sample" Reference only.

5.5 CuO

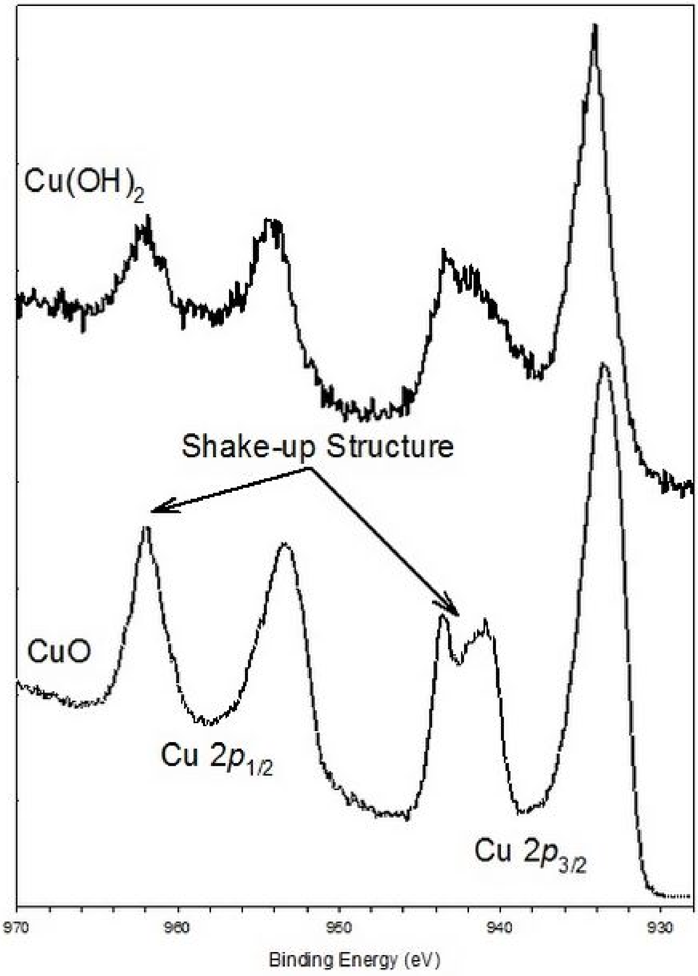

CuO formation (bottom), including satellite[29].

5.6 Uncertainty Example

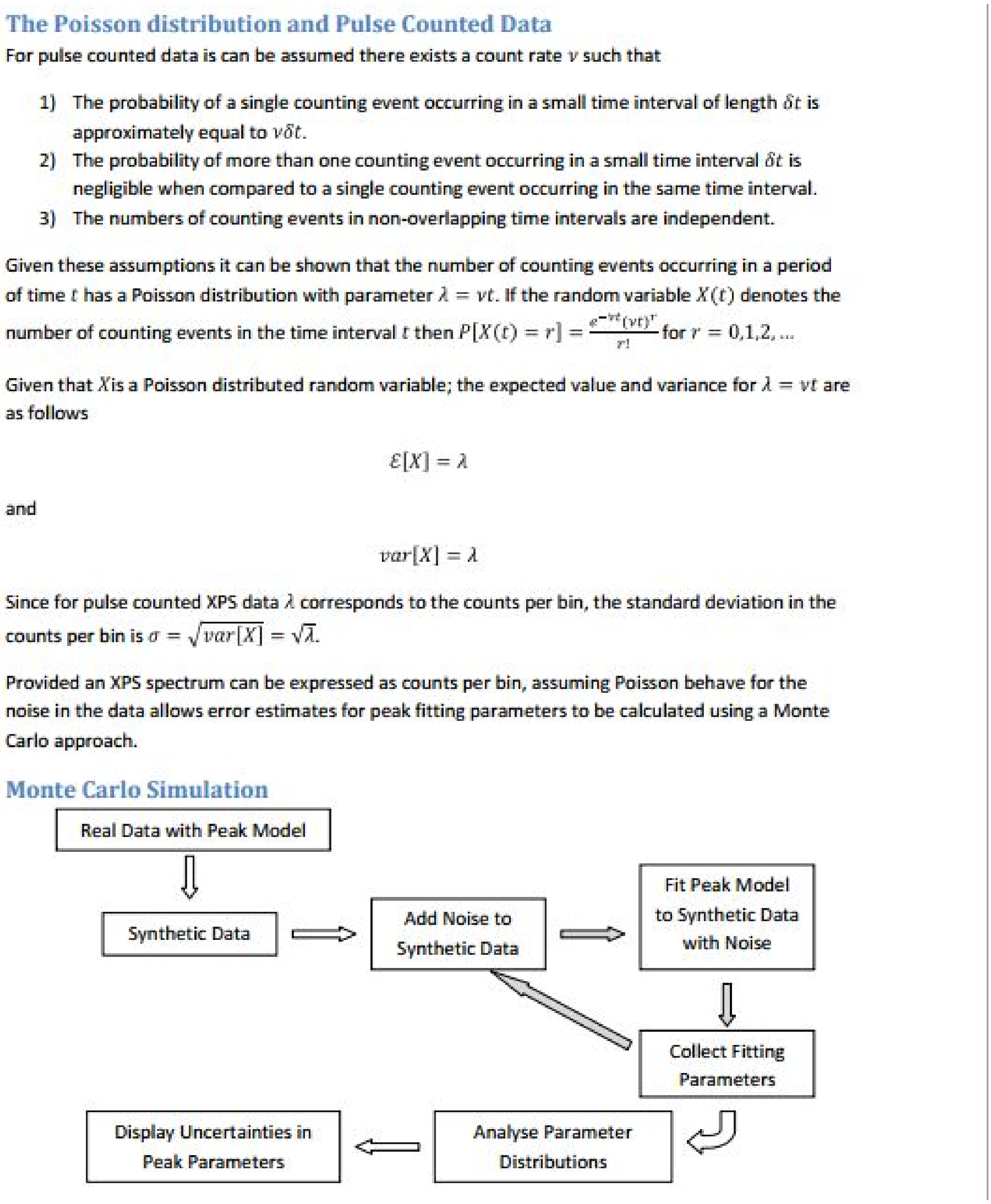

The Poisson distribution and Pulse Counted Data

For pulse counted data is can be assumed there exists a count rate ν such that

1) The probability of a single counting event occurring in a small time interval of length δt is approximately equal to $\nu\delta t$.
2) The probability of more than one counting event occurring in a small time interval δt is negligible when compared to a single counting event occurring in the same time interval.
3) The numbers of counting events in non-overlapping time intervals are independent.

Given these assumptions it can be shown that the number of counting events occurring in a period of time t has a Poisson distribution with parameter $\lambda = \nu t$. If the random variable $X(t)$ denotes the number of counting events in the time interval t then $P[X(t) = r] = \frac{e^{-\nu t}(\nu t)^r}{r!}$ for $r = 0,1,2, \ldots$

Given that $X$is a Poisson distributed random variable; the expected value and variance for $\lambda = \nu t$ are as follows

$$\mathcal{E}[X] = \lambda$$

and

$$var[X] = \lambda$$

Since for pulse counted XPS data λ corresponds to the counts per bin, the standard deviation in the counts per bin is $\sigma = \sqrt{var[X]} = \sqrt{\lambda}$.

Provided an XPS spectrum can be expressed as counts per bin, assuming Poisson behave for the noise in the data allows error estimates for peak fitting parameters to be calculated using a Monte Carlo approach.

Monte Carlo Simulation

Basic example of how CasaXPS can calculate uncertainty on compositional values [27].